

Simulated predictions for H I at $z = 3.35$ with the Ooty Wide Field Array - I. Instrument and the foregrounds

Visweshwar Ram Marthi^{1*}, Suman Chatterjee^{2,3}, Jayaram N Chengalur¹,
Somnath Bharadwaj^{2,3}

¹*National Centre for Radio Astrophysics, Tata Institute of Fundamental Research, Post Bag 3, Ganeshkhind, Pune - 411 007, India*

²*Department of Physics and Meteorology, Indian Institute of Technology Kharagpur, Kharagpur - 721 302, India*

³*Centre for Theoretical Studies, Indian Institute of Technology Kharagpur, Kharagpur - 721 302, India*

Accepted 2017 July 14. Received 2017 June 25; in original form 2016 November 22

ABSTRACT

Foreground removal is the most important step in detecting the large-scale redshifted H I 21-cm signal. Modelling foreground spectra is challenging and is further complicated by the chromatic response of the telescope. We present a multi-frequency angular power spectrum (MAPS) estimator for use in a survey for redshifted H I 21-cm emission from $z \sim 3.35$, and demonstrate its ability to accurately characterize the foregrounds. This survey will be carried out with the two wide-field interferometer modes of the upgraded Ooty Radio Telescope, called the Ooty Wide Field Array (OWFA), at 326.5 MHz. We have tailored the two-visibility correlation for OWFA to estimate the MAPS and test it with simulated foregrounds. In the process, we describe a software model that encodes the geometry and the details of the telescope, and simulates a realistic model for the bright radio sky. This article presents simulations which include the full chromatic response of the telescope, in addition to the frequency dependence intrinsic to the foregrounds. We find that the visibility correlation MAPS estimator recovers the input angular power spectrum accurately, and that the instrument response to the foregrounds dominates the systematic errors in the recovered foreground power spectra.

Key words: instrumentation: interferometers; methods: data analysis, numerical, statistical; techniques: interferometric; cosmology: observations, diffuse radiation, large-scale structure of Universe

1 INTRODUCTION

Measuring the post-reionisation neutral hydrogen power spectrum provides a new probe of the large scale structure of the universe (Bharadwaj et al. 2001; Wyithe & Loeb 2009; Pritchard & Loeb 2012), and would allow constraining many important cosmological parameters (Wyithe et al. 2008; Loeb & Wyithe 2008; Bharadwaj et al. 2009; Visbal et al. 2009; Chang et al. 2010; Seo et al. 2010; Bull et al. 2015; Padmanabhan et al. 2015). The surge of interest in 21-cm intensity mapping over the last decade stems from the promise of constraining dark energy. The expansion of the universe is thought to accelerate at late times due to dark energy. The Baryon Acoustic Oscillation (BAO) has been proposed as a standard ruler (Eisenstein 2005). Its measurement at multiple redshifts can measure the rate of expansion of the universe over cosmic time and hence

place constraints on dark energy (Wang 2006; Chang et al. 2008). More recently, 21-cm intensity mapping has gained attention due to its potential to constrain the neutrino masses (e.g. Pritchard & Pierpaoli 2008, 2009; Oyama et al. 2013; Villaescusa-Navarro et al. 2015). A number of post-reionisation experiments are currently being planned: interferometric experiments, like the Canadian Hydrogen Intensity Mapping Experiment (CHIME; Bandura et al. 2014) and those with other telescopes such as the Ooty Wide Field Array (OWFA; Prasad & Subrahmanya 2011; Subrahmanya et al. 2017), the Baryon Acoustic Oscillation Broadband and Broad Beam Array (BAOBAB; Pober et al. 2013a), and the Tianlai Cylinder Radio Telescope (CRT; Chen 2011), as well as single dish intensity mapping experiments like BINGO (Battye et al. 2016) and GBT-HIM (e.g. Chang et al. 2010). The goals of these experiments are similar - to constrain cosmological parameters through a measurement of the power spectrum of the redshifted H I 21-cm signal and to measure the BAO peak through a measure-

* E-mail: vrmarthi@ncra.tifr.res.in

ment of the power spectrum of the density fluctuations. This article discusses the OWFA effort.

Ali & Bharadwaj (2014) have presented calculations of both the H I signal and the foregrounds expected for OWFA, considering the diffuse Galactic synchrotron and the extragalactic radio source contribution. Bharadwaj et al. (2015) present Fisher-matrix forecasts of the H I signal for OWFA, where they predict that a 5σ detection of the amplitude of H I signal is achievable in ~ 150 hours of integration, assuming that foregrounds have been completely removed.

The 39-MHz observing band at OWFA, centred at 326.5 MHz, provides access to the H I signal from a window of $\Delta z \sim 0.52$ around $z \sim 3.35$. A statistical detection of the post-reionisation signal is fraught with challenges very similar to those in low frequency radio epoch of reionisation (EoR) experiments, the most formidable of which is dealing foreground emission (see e.g. Furlanetto et al. 2006; Ali et al. 2008). Foregrounds are important at least for two reasons: (1) the astrophysical foregrounds are many orders of magnitude brighter than the cosmological signal, and (2) foregrounds interact with the instrument to produce spectral signatures that can contaminate the H I signal (see e.g. Vedantham et al. 2012; Thyagarajan et al. 2015a).

At least two classes of techniques to treat foregrounds exist. In foreground removal methods, the foregrounds are mathematically modelled as spectrally smooth functions and subtracted in the image space (Morales et al. 2006; Jelić et al. 2008; Bowman et al. 2009; Liu et al. 2009b; Chapman et al. 2012) or from the visibilities (McQuinn et al. 2006; Gleser et al. 2008; Liu et al. 2009a; Petrovic & Oh 2011). Ghosh et al. (2011a,b) fit smooth functions to the multi-frequency angular power spectrum at each multipole to subtract the foregrounds, exploiting the fact that the H I signal decorrelates more rapidly with frequency (Bharadwaj & Sethi 2001; Bharadwaj & Ali 2005) than the foregrounds. Foreground isolation, on the other hand (Datta et al. 2010; Morales et al. 2012; Parsons et al. 2012; Vedantham et al. 2012; Thyagarajan et al. 2013; Liu et al. 2014), uses only those regions of the observed \mathbf{k} -space that can be identified as being less affected by the foreground emission.

Although it is known that the major foreground components all have smooth spectral behaviour, allowing them to be distinguished from the cosmological 21-cm signal, the telescope's chromatic response introduces spectral features in the foreground contribution to the observed signal. These effects, the details of which are telescope-specific, pose a serious challenge for any foreground removal technique. Simulations that incorporate a detailed frequency dependent telescope model are crucial to quantifying these effects as well validating any foreground removal technique. In this paper we present a software emulator that describes a chromatic model for OWFA. The emulator is used in conjunction with a foreground sky model to predict the foregrounds expected in observations with OWFA. The three dimensional power spectrum $P(\mathbf{k})$ of the redshifted 21-cm brightness temperature fluctuations (e.g. Bharadwaj & Ali 2005) is well suited to quantifying the H I signal which, to a good approximation, may be assumed statistically homogeneous in the three dimensional space spanned by the two angular coordinates and the frequency axis. This assumption, however, is not valid for the foregrounds, where the statis-

tics are quite different in the angular and frequency directions. The issue is further complicated by the telescope's chromatic response. The Fourier modes \mathbf{k} are no longer the ideal basis, and the power spectrum $P(\mathbf{k})$ is no longer the obvious choice to quantify the statistical properties of the measured sky signal. In this paper we propose using the correlations between the visibilities to quantify the statistical properties of the measured sky signal. The relation between the visibility correlations and the power spectrum $P(\mathbf{k})$ has been studied in several earlier works (Bharadwaj & Sethi 2001; Bharadwaj & Ali 2005; Ali & Bharadwaj 2014) and is well understood. The multi-frequency angular power spectrum (MAPS; Datta, Choudhury & Bharadwaj 2007) provides a technique to jointly characterize the angular and frequency dependence of the observed sky signal. This is very closely related to the visibility correlations (Ali et al. 2008; Ali & Bharadwaj 2014), and we also use this to quantify our simulated foreground predictions for OWFA. In what follows we distinguish between three different kinds of visibilities, viz.: (a) the model visibilities, which are the Fourier transform of the primary beam-weighted sky brightness distribution for the array geometry under consideration, (b) the measured visibilities, which are the actual measurements of the beam-weighted sky made by the array, corrupted by the complex antenna gains and (c) the true visibilities, which are obtained from the measured visibilities after the process of calibration, which is a noisy version of the model visibilities.

To begin with, we introduce OWFA, the instrument, in Section 2, and describe the emulator in Section 3. In Section 4 we introduce the foreground components and describe the steps in the simulation of the foreground fields. The model visibilities are obtained for the simulated foregrounds, given the instrument description. Section 5 introduces the multi-frequency angular power spectrum (MAPS) estimator and its construction from the visibility correlation for OWFA, which we use to estimate the angular power spectrum from the true visibilities. Section 6 presents the results of the simulation and power spectrum estimation. We follow them up with a discussion of the properties of the estimator in Section 7.

2 THE OOTY WIDE FIELD ARRAY - OWFA

The Ooty Radio Telescope (ORT; Swarup et al. 1971) is located in the Nilgiri Hills in the Indian peninsula, approximately at 11°N at an altitude of $\sim 8,000$ ft. The telescope, operating at 326.5 MHz, has an offset-parabolic cylindrical reflector whose aperture is a 530 m long and 30 m wide rectangle as shown in Figure 2. The feed consists of 1056 dipoles, each 0.5λ long, all arranged end to end along the length of the line focus of the reflector. The telescope is located on a hill that is roughly sloped 11° North-South, which equals the latitude of the station. Figure 1 shows a part of the ORT. Effectively, the axis of the cylinder is parallel to the earth's rotation axis, making it equatorially mounted. The telescope is steerable in the East-West direction mechanically by rotating the cylinder about its axis, allowing continuous tracking of a source on the sky from rise to set. The telescope's response is steered electronically in the North-South direction by switching the phases of the dipoles through an analog phase-switching network. Here we consider observations



Figure 1. (colour online) A photograph of the Ooty Radio Telescope (ORT) on the sloping hill, showing four of the 22 parabolic frames. The left side of the picture is North and the right is South.

pointed towards the phase center $(\alpha, \delta) = (\alpha_0, \delta_0)$, denoted by the unit vector \mathbf{m} (Figure 2).

In the legacy ORT system the signals from the dipoles are combined in a passive combiner network tree, only a part of which is shown Figure 3. The signals from 24 successive dipoles are combined hierarchically in a series of 4-way, 2-way and 3-way combiners. The output at this stage is called a half-module. Two half-module outputs are again combined in a 2-way combiner: therefore the 1056 dipoles are grouped into 22 modules of 48 dipoles each. The 22 modules are split into 11 Northern and 11 Southern modules, each half is used to generate 11 phase-shifted beams, each pointing at a different direction, and 1 total intensity beam. The beams obtained from the Northern and Southern modules are correlated with each other to get rid of systematics. The legacy beam-former mode of the ORT system provides twelve simultaneous beams on the sky.

The ORT is presently undergoing a major upgrade to operate as a programmable interferometer (Subrahmanya et al. 2017). The upgrade will enable two concurrent but independent interferometer modes, besides retaining the workhorse beam-former mode. The two concurrent modes are:

(i) P-II : the signal is tapped after the 4-way combiner - the second stage of the combiner network (Figure 3) - to give a field-of-view (FoV) of $1.8^\circ \times 27^\circ$ EW \times NS and a bandwidth of ~ 39 MHz. It would operate as a linear array of 264 equi-spaced antennas, giving $\sim 35,000$ baselines.

(ii) P-I: every group of six adjacent 4-way combiner outputs are summed in phase in the software correlator system. This is equivalent to the signal being tapped at every half-module (24 dipoles), giving a FoV of $1.8^\circ \times 4.5^\circ$ EW \times NS, and ~ 39 MHz bandwidth. It would operate as an independent linear array of 40 equi-spaced antennas, giving 780 baselines.

The RF signals tapped at the 4-way combiner (Figure 3) are digitised in the field and the signals are transported to the central building on optical fibre. The signals undergo two levels of pooling and a protocol conversion before arriving in a high-performance cluster (HPC) that will correlate the

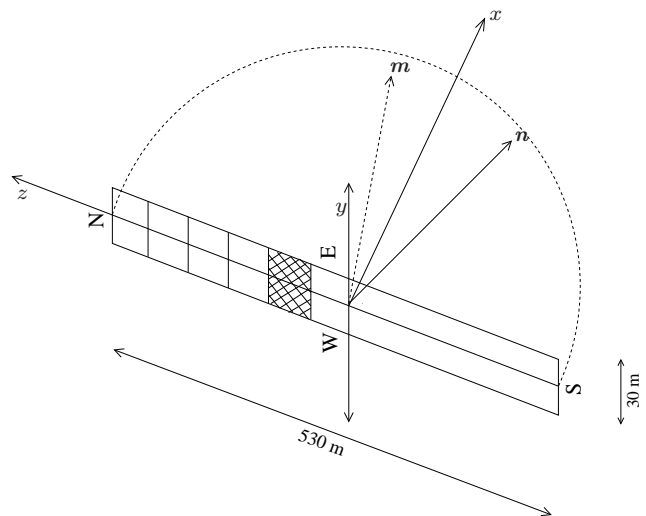


Figure 2. This shows a diagram of the $30\text{m} \times 530\text{m}$ aperture of the ORT parabolic cylinder whose axis is aligned with the N-S direction. The smaller rectangles, one of which is shaded, depict the apertures of the individual OWFA antennas which are linearly arranged along the length of the ORT cylinder. The unit vector \mathbf{n} denotes an arbitrary direction with coordinates (α, δ) on the celestial sphere. Our Cartesian coordinate system which is tied to the telescope has the z -axis in the N-S direction, and the x -axis along the normal to the aperture pointing towards the position $(\alpha_0, 0)$ on the celestial equator. The unit vector \mathbf{m} denotes the phase center (α_0, δ_0) which can be steered electronically in the N-S direction.

signals to obtain the visibilities. The P-I system mentioned above will run in parallel with the P-II system within the HPC.

OWFA will operate as an array of N_A antennas arranged linearly along the length of the 530 m ORT cylinder as shown in Figure 2. Each OWFA antenna has a $b \times d$ rectangular aperture, where $b = 30$ m is the width of the parabolic reflector and d is the length of the antenna which is different for P-I and P-II. d is also the spacing between an adjacent antenna pair. The array parameters are summarized in Table 1.

The regular spacing of the antennas results in a large fraction of the ${}^N A C_2^1$ baselines being redundant, and there are only $N_A - 1$ unique baselines. We can express these unique baselines in terms of the smallest baseline $\mathbf{U}_1 = d\nu/c$ as

$$\mathbf{U}_n = n \mathbf{U}_1 \quad \text{with } 1 \leq n \leq N_A - 1. \quad (1)$$

Each baseline \mathbf{U}_n has a redundancy factor of $N_A - n$.

OWFA is conveniently described using a right-handed Cartesian coordinate system tied to the telescope as shown in Figure 2. The z -axis is along the N-S direction which is parallel to the axis of the parabolic cylinder, and the x -axis is normal to the telescope's aperture. In this coordinate system the baseline vectors are all along the z -axis and we have

$$\mathbf{U}_n = |U_n| \mathbf{z}. \quad (2)$$

¹ ${}^n C_r$ is defined as $\frac{n!}{(n-r)!r!}$

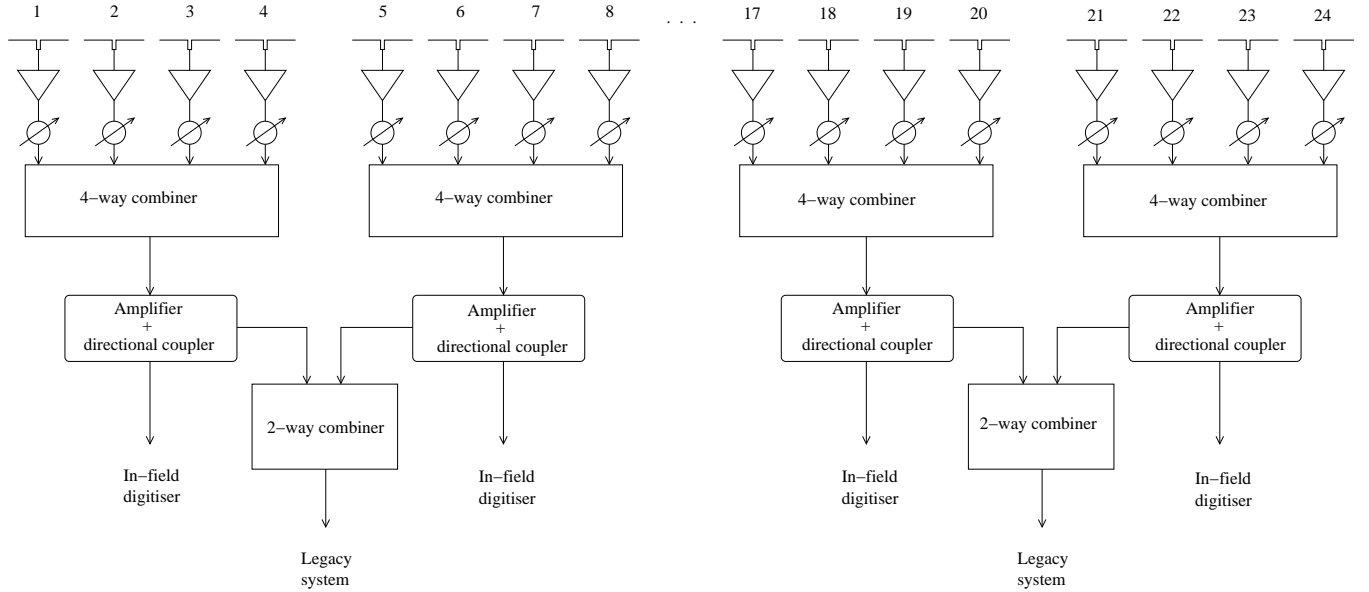


Figure 3. The signal paths from the dipoles to the digitiser of OWFA: each dipole has an LNA and a phase shifter for setting the declination. The output of the 2-way combiner proceeds to the legacy ORT receiver system. The legacy ORT receiver system is a beam-former network capable of producing twelve simultaneous beams on the sky.

The unit vector \mathbf{n} towards an arbitrary direction (α, δ) on the celestial sphere can be expressed as

$$\mathbf{n} = \sin(\delta) \mathbf{z} + \cos(\delta) [\cos(\alpha - \alpha_0) \mathbf{x} + \sin(\alpha - \alpha_0) \mathbf{y}]. \quad (3)$$

where \mathbf{x} , \mathbf{y} and \mathbf{z} respectively denote the unit vectors along the x -, y - and z -axes. The unit vector \mathbf{m} towards the phase center (α_0, δ_0) can be represented as

$$\mathbf{m} = \sin(\delta_0) \mathbf{z} + \cos(\delta_0) \mathbf{x}. \quad (4)$$

Observations at 326.5 MHz relate to H I at $z = 3.35$, which is at a comoving distance of $r = 6.84$ Gpc. This relates each baseline \mathbf{U} to $k_{\perp} = \frac{2\pi|\mathbf{U}|}{r}$ which is the component of a 3D wave vector \mathbf{k} perpendicular to \mathbf{m} . This sets the range k_{\perp}^{\min} and k_{\perp}^{\max} that will be probed by OWFA (Ali & Bharadwaj 2014). Since OWFA is one-dimensional, it only probes k_{\perp} along the length of the interferometer. We also have $r' = |dr/d\nu| = 11.5 \text{ Mpc MHz}^{-1}$ which sets the comoving interval $L = r' B_{\text{bw}}$ spanned by B_{bw} the system bandwidth of OWFA. This sets $k_{\parallel}^{\min} = \frac{2\pi}{r' B_{\text{bw}}}$ and $k_{\parallel}^{\max} = \frac{\pi}{r' (\Delta\nu)}$ where $\Delta\nu$ is the channel width (frequency resolution) and k_{\parallel} is the component of \mathbf{k} parallel to \mathbf{m} . Table 1 summarizes the important parameters of the two interferometer modes, assuming the *WMAP* 9-year results for the cosmological parameters (Hinshaw et al. 2013).

3 A SOFTWARE EMULATOR FOR OWFA

In this Section, we will describe a software emulator for OWFA that we subsequently use to make foreground predictions. The emulator (**Prowess**; Marthi 2017) was written (1) to simulate the observed radio sky at 327 MHz, (2) to provide a pipeline to simulate visibilities, introduce extrinsic systematics, study intrinsic systematics and allow us to test calibration schemes (see Marthi & Chengalur 2014) and

Table 1. Parameters of OWFA. OWFA is a one-dimensional interferometer; the values for k pertain only to the north-south extent of the array elements.

Parameter	P-I	P-II
Antennas	40	264
Total baselines	780	34716
Unique baselines	39	263
Shortest baseline	11.5 m	1.92 m
Longest baseline	448.5 m	505.0 m
Central frequency	326.5 MHz	326.5 MHz
Bandwidth	39 MHz	39 MHz
Spectral resolution	125 kHz	125 kHz
Aperture ($b \times d$)	$30 \times 11.5 \text{ m}^2$	$30 \times 1.97 \text{ m}^2$
FoV at $\delta = 0^\circ$	$1.8^\circ \times 4.5^\circ$	$1.8^\circ \times 27^\circ$
Resolution	$0.1^\circ \text{ sec } \delta_0 \times 1.8^\circ$	$0.1^\circ \text{ sec } \delta_0 \times 1.8^\circ$
k_{\perp}^{\min}	$1.1 \times 10^{-2} \text{ Mpc}^{-1}$	$2.0 \times 10^{-3} \text{ Mpc}^{-1}$
k_{\perp}^{\max}	$4.6 \times 10^{-1} \text{ Mpc}^{-1}$	$5.2 \times 10^{-1} \text{ Mpc}^{-1}$
k_{\parallel}^{\min}	$1.4 \times 10^{-2} \text{ Mpc}^{-1}$	$1.4 \times 10^{-2} \text{ Mpc}^{-1}$
k_{\parallel}^{\max}	4.6 Mpc^{-1}	4.6 Mpc^{-1}

detection strategies even as the telescope undergoes an upgrade, (3) to prepare a science-ready observatory data analysis software pipeline in time for first light. For the purpose of this article, only the first and second items are relevant. We describe **Prowess**² and some of the details of its design briefly in this section. It is important to note that the telescope model incorporated in the emulator includes the chromatic effects associated with the primary beam and the baselines.

² **Prowess** is available at <https://github.com/vrmarthi/prowess>

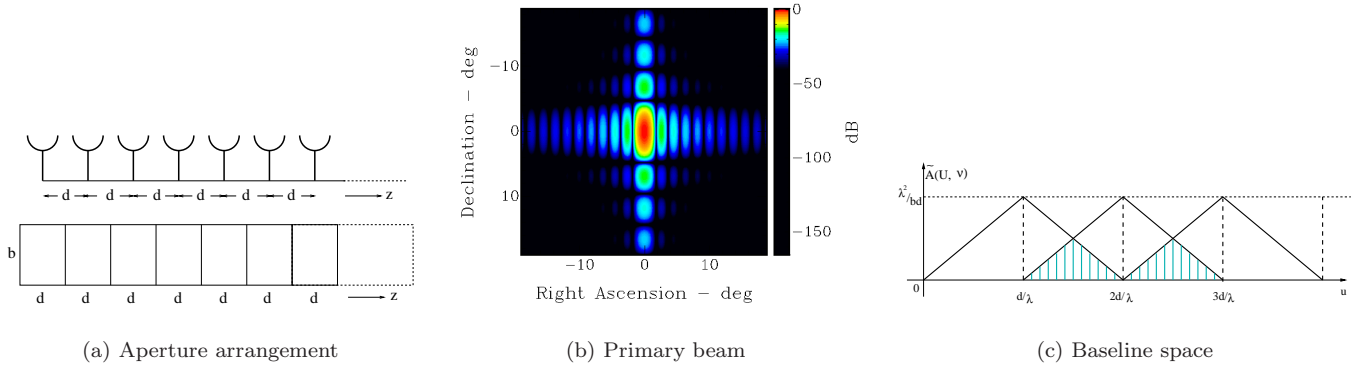


Figure 4. (colour online) The aperture arrangement for OWFA in real and baseline space.

3.1 Visibilities

The visibilities $\mathbf{M}(\mathbf{U})$ are the Fourier transform of the product of the specific intensity distribution on the sky $I(\mathbf{n}, \nu)$ and the telescope's primary beam pattern $A(\Delta\mathbf{n}, \nu)$ where $\Delta\mathbf{n} = \mathbf{n} - \mathbf{m}$ (Figure 2). The visibilities can be calculated as

$$\mathbf{M}(\mathbf{U}) = \int d\Omega_{\mathbf{n}} I(\mathbf{n}, \nu) A(\Delta\mathbf{n}, \nu) e^{-2\pi i \mathbf{U} \cdot \Delta\mathbf{n}} \quad (5)$$

where the solid angle integral is over the entire celestial hemisphere.

Here $A(\Delta\mathbf{n}, \nu)$ is the primary beam power pattern of OWFA, modelled as a two-dimensional sinc-squared function

$$A(\Delta\mathbf{n}, \nu) = \text{sinc}^2\left(\frac{\pi b \nu \Delta n_y}{c}\right) \text{sinc}^2\left(\frac{\pi d \nu \Delta n_z}{c}\right) \quad (6)$$

where Δn_y and Δn_z are respectively the y and z components of $\Delta\mathbf{n}$. The primary beam pattern here is taken to be the diffraction pattern of rectangular aperture of dimensions $b \times d$, the values of b and d for OWFA are given in Table 1. This form of the primary beam has been assumed as it likely to lead to larger systematics because of its high sidelobe levels and is hence conservative. In reality, the tapered east-west illumination of the aperture results in an approximately truncated Gaussian beam. **Prowess** is capable of handling any user-defined primary beam. Figure 4(a) shows the aperture arrangement and Figure 4(b) shows the P-I primary beam pattern as a function of the celestial coordinates α and δ for a pointing towards $(\alpha_0, \delta_0) = (0, 0)$.

Note that in this co-ordinate system the phase factor which is the argument of the exponent in equation (5)

$$2\pi i \mathbf{U} \cdot \Delta\mathbf{n} = 2\pi i |\mathbf{U}| [\sin(\delta) - \sin(\delta_0)] \quad (7)$$

depends only on the baseline length and the declinations, reflecting the 1D geometry of OWFA.

3.2 Overview of the software pipeline

We begin with a geometric description of the array in an input Antenna Definition file. Since the telescope is equatorially mounted, the baseline co-ordinates remain stationary as the antennas track the pointing coordinates on the sky. The baseline vectors are obtained from the physical antenna

separations defined at the central frequency but scaled appropriately at each channel when computing the visibilities.

$$\mathbf{d}_{|a-b|} = \mathbf{x}_a - \mathbf{x}_b, \quad \mathbf{U}_{|a-b|} = \mathbf{d}_{|a-b|} \frac{\nu}{c} \quad (8)$$

It is worth noting that the chromatic response of the interferometer enters the picture through equations (6) and (8) which respectively capture the fact that the primary beam pattern and the baseline distribution both vary with frequency. Even for a perfectly achromatic source, the chromatic response of the interferometer will introduce a frequency dependent structure in the measured visibilities.

The pixel sizes in all our simulated maps and the primary beam are $\sim 1' \times 1'$. The maps and the primary beam are all 2048×2048 pixels wide, spanning an angular extent of $\sim 38^\circ$ in each dimension. In this paper, we will focus only on P-I, where the antenna primary beam full width at half maximum (FWHM) is $1.8^\circ \times 4.5^\circ$.

The brightness distribution for the diffuse foreground component in our simulations is obtained as a random realisation of its power spectrum (see Section 4). The specific intensities $I(\mathbf{n}_p, \nu)$ of the pixelized sky map are converted to flux densities by scaling with the appropriate solid angle

$$S(\mathbf{n}_p, \nu) = I(\mathbf{n}_p, \nu) \Delta\Omega, \quad (9)$$

the index p here refers to the N_P pixels in the map. The extragalactic point source foreground is obtained as a random realisation of its power spectrum and obeying the differential source count relation (see Section 4). This results in a set of N_S discrete extragalactic radio sources identified by their respective positions \mathbf{n}_s and flux densities $S(\mathbf{n}_s, \nu)$.

We note that similar simulations of both the instrument and foregrounds have been carried out for CHIME (Shaw et al. 2014) and MWA (Thyagarajan et al. 2015a). In contrast to the above full sky foreground simulations we emphasize that for P-I of OWFA, where the primary beam is much smaller in comparison, a full sky treatment of the foregrounds is not necessary. However, unlike the small FoV LOFAR foreground simulations (Jelić et al. 2008), we do consider a FoV much further out than the primary. For P-II, with a primary FoV of 0.5 rad, wide-field effects become important, and they will be considered separately for the P-II forecasts.

The model visibilities $\mathbf{M}(\mathbf{U})$ for the non-redundant set

of baselines are obtained using a discretised version of equation (5):

$$\mathbf{M}(\mathbf{U}) = \sum_b S(\mathbf{n}_b, \nu) A(\Delta\mathbf{n}_b, \nu) e^{-i2\pi\mathbf{U}\cdot\Delta\mathbf{n}_b}. \quad (10)$$

The sum denoted here by the index b includes the N_P pixels of the diffuse foreground as well as the N_S discrete extragalactic sources.

The visibility \mathbf{V} measured by a baseline with antennas a and b depends on the model visibility for that particular spacing, as well the element gains:

$$\mathbf{V}(\mathbf{U}_{ab}) = g_a g_b^* \mathbf{M}(\mathbf{U}_{|a-b|}) + \mathcal{N}(\mathbf{U}_{ab}) \quad (11)$$

where g_a and g_b are the complex antenna gains (which could also be frequency dependent) and \mathcal{N} is Gaussian random noise equivalent to the system temperature T_{sys} .

The antenna gains and the true (calibrated) visibilities are estimated from the measured visibilities by employing the non-linear least squares minimisation algorithm described in [Marthi & Chengalur \(2014\)](#). Due to the enormous redundancy of the measurements, the highly overdetermined system of equations enables simultaneously solving for both the gains and the true visibilities. This is interesting particularly in light of studies regarding the limitations introduced by calibration based on an incomplete model of the sky, as is routinely employed in interferometry [Patil et al. \(2016\)](#). The real and imaginary part of the noise \mathcal{N} in equation (11) each has a RMS fluctuation ([Thompson et al. 2008](#))

$$\sigma_{ab} = \frac{\sqrt{2}k_B T_{\text{sys}}}{\eta A \sqrt{\Delta\nu \Delta t}} \quad (12)$$

per channel, where k_B is the Boltzmann constant, η is the aperture efficiency, $A = b \times d$ is the aperture area, $\Delta\nu$ the channel width and Δt the integration time. The foreground maps give the flux in Jy units at every pixel, therefore the Fourier sum directly produces the model visibilities in Jy units. The flowchart in Figure 7 of [Marthi \(2017\)](#) gives an overview of the part of the emulator used to obtain the visibilities. As mentioned earlier, the emulator fully incorporates the chromatic response of the instrument. The baselines (eq. 8), the primary beam (eq. 6) and the sky vary with frequency. These quantities were calculated separately at each frequency and used in equation (10) to calculate the visibilities. The spectral variation of the sky is discussed in Section 4. The pixel solid angle $\Delta\Omega$ in equation (9) is held fixed across the band. In our simulations of the foregrounds, the sky is sampled at a much higher resolution than the resolution element of OWFA. The simulated visibilities, the primary beam and the foreground maps are written to disk in the Flexible Image Transport System (FITS; [Wells et al. 1981](#)) format. The visibility records are written to UVFITS files at one-second interval.

In **Prowess**, the observing band is centred at 326.5 MHz with a bandwidth of ~ 39 MHz split into 312 channels in the simulations. The frequency resolution is thus 125 kHz per channel. Based on our understanding of the distribution of the neutral gas around the redshift of $z \sim 3.35$, the H I signal at two redshifted frequencies, separated by more than $\Delta\nu \sim 1$ MHz, is expected to decorrelate rapidly ([Bharadwaj & Ali 2005](#); [Bharadwaj et al. 2009](#); [Chatterjee et al. 2017](#)). This means that with a channel resolution of 125 kHz, the H I signal correlation is adequately

sampled over the 1-MHz correlation interval. In reality, the channel resolution is likely to be much finer (~ 50 kHz), with about 800 channels across the 39-MHz band. This is useful for the identification and excision of narrow line radio frequency interference. Beyond the need to handle RFI, there is no incentive to retaining the visibilities at this resolution. Eventually, we may smooth the data to a resolution of 125 kHz, keeping in mind the decorrelation bandwidth of the H I signal. **Prowess** itself is indeed capable of running at any frequency resolution, including the actual final configuration of the P-I and P-II systems. But the 125-kHz resolution used in the simulations allows for rapid processing, especially if they are to be run repetitively for a wide range of different parameters.

4 THE FOREGROUNDS

The most dominant contributors to the foregrounds are the diffuse synchrotron emission from our Galaxy and the extragalactic radio sources (see e.g. [Di Matteo et al. 2002](#); [Santos et al. 2005](#); [Furlanetto et al. 2006](#); [Ali et al. 2008](#)). Although some choice is available in the selection of a reasonably cold region of the Galaxy through which to observe the distant universe, emission from extragalactic radio sources is ubiquitous. At different angular scales, either of the two dominates: at the very large scales, $\ell \lesssim 100$, the Galactic synchrotron emission contributes more to the foreground budget. At smaller scales, there is a gradual transition to the flux from extragalactic sources. Galactic synchrotron is likely to dominate the emission at the largest angular scales observable by P-II at the OWFA, and likely at the first few baselines of P-I ([Ali & Bharadwaj 2014](#)) at higher declinations. Since the largest contribution to the H I signal is expected to come from the largest angular scales ([Chatterjee et al. 2017](#)) we would have access to, the large scale emission from the diffuse foreground assumes importance.

4.1 The Diffuse Galactic Foreground

Diffuse synchrotron emission from the Galaxy has been studied extensively, both within the context of statistical H I experiments ([Jelić et al. 2008](#); [Bernardi et al. 2009](#); [Jelić et al. 2014](#)) as well as in their own right (e.g. [Haslam et al. 1981, 1982](#)). [La Porta et al. \(2008\)](#) determine the power spectrum of the diffuse synchrotron emission at scales larger than 0.5° from the 408-MHz Haslam total intensity maps, where they find that the index of the power law γ varies between 2.6 and 3.0. Similarly, there are measurements at scales smaller than 0.5° from the WSRT ([Bernardi et al. 2009, 2010](#)), GMRT ([Ghosh et al. 2012](#)) and LOFAR ([Iacobelli et al. 2013](#)).

We assume that the fluctuations in the diffuse Galactic Synchrotron radiation are statistically homogeneous and isotropic, described by a Gaussian random field whose statistical properties are completely specified by the angular power spectrum. We further assume that the input model angular power spectrum $C_\ell^M(\nu)$ is well described by a single power law in the entire range of angular scales of our interest

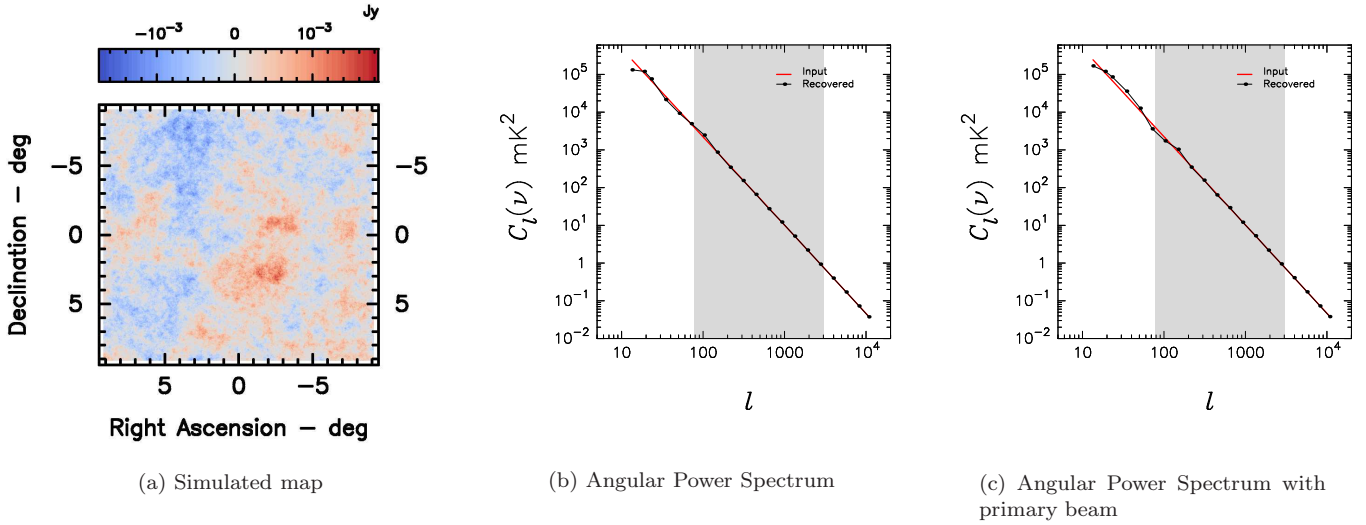


Figure 5. (colour online) (a) shows a particular realization of the simulated brightness temperature map $\delta T(\boldsymbol{\theta}, \nu)$ in (α, δ) coordinates for the nominal frequency of $\nu = 326.5$ MHz. In (b) the black points show the angular power spectrum recovered from the simulated map shown in (a), the input model angular power spectrum $C_\ell^M(\nu)$, is shown by the curve in red. The shaded region shows the multipole range $\ell_{\min} - \ell_{\max}$ accessible to OWFA. (c) shows the angular power spectrum recovered by applying equation (16) to the image obtained for a single realisation by multiplying the simulated map (a) with the primary beam pattern shown in Figure 4(b).

(e.g. Santos et al. 2005; Ali et al. 2008):

$$C_\ell^M(\nu) = A_{\nu_0} \left(\frac{\nu_0}{\nu}\right)^{2\alpha} \left(\frac{1000}{\ell}\right)^\gamma \quad (13)$$

where A_{ν_0} is a constant - the amplitude that can be determined observationally at ν_0 (here at $\ell = 1000$), α is the spectral index and γ is the index of the spatial power.

A map of the diffuse synchrotron radiation can be obtained as a realization of a Gaussian random field whose power is distributed in the angular scales described by eqn (13). A detailed description of how to generate such a realization can be found in Choudhuri et al. (2014), but we give a brief summary here for completeness. Consider the model angular power spectrum given in equation (13). We take $A_{150} = 513 \text{ mK}^2$, which is the amplitude of the angular power spectrum measured at 150 MHz with the GMRT (Ghosh et al. 2012). For the other parameters, we take $\alpha = 2.52$ (Rogers & Bowman 2008) and $\gamma = 2.34$ (Ghosh et al. 2012). The spectral index α scales the observed brightness temperature from a 150-MHz observation to 326.5 MHz as well as imparts an in-band spectral shape to the diffuse emission.

The foreground simulations have been carried out under the flat sky approximation with $\mathbf{n} = \mathbf{m} + \boldsymbol{\theta}$, where $\boldsymbol{\theta}$ is a 2D vector on the plane of the sky. We use \mathbf{U} to denote the Fourier modes corresponding to $\boldsymbol{\theta}$, and these are related to the angular multipole ℓ as $\ell = 2\pi|\mathbf{U}|$. The Fourier components of the brightness temperature fluctuations are generated on a grid through

$$\Delta\tilde{T}(\mathbf{U}, \nu) = \sqrt{\frac{\Omega C_\ell^M(\nu)}{2}} (x + iy), \quad (14)$$

where Ω is the total solid angle of the simulated field, and x and y are independent Gaussian random variables with zero mean and unit variance. The map of the brightness

temperature fluctuations $\delta T(\boldsymbol{\theta}, \nu)$, or equivalently the specific intensity fluctuations $\delta I(\mathbf{n}, \nu)$, is obtained through a Fourier inversion. Figure 5(a) shows a single realization of the simulated brightness temperature map in $\delta T(\boldsymbol{\theta}, \nu)$ in (α, δ) coordinates, for which the recovered angular power spectrum $C_\ell(\nu)$ is shown in Figure 5(b) in comparison with the input model $C_\ell^M(\nu)$ used to obtain the random realization. The simulated map is multiplied with the OWFA primary beam pattern (Figure 4(b)) to obtain $\delta T_B(\boldsymbol{\theta}, \nu) = \delta T(\boldsymbol{\theta}, \nu) A(\boldsymbol{\theta}, \nu)$ which is used to calculate the model visibilities (equation 10). Here $\Delta\tilde{T}_B(\mathbf{U})$, which is the Fourier transform of $\delta T_B(\boldsymbol{\theta}, \nu)$, is related to the angular power spectrum $C_\ell(\nu)$ as

$$\langle |\Delta\tilde{T}_B(\mathbf{U})|^2 \rangle = \int d^2 \mathbf{U}' |\tilde{A}(\mathbf{U} - \mathbf{U}')|^2 C_{\ell'}(\nu) \quad (15)$$

where $\ell' = 2\pi|\mathbf{U}'|$ and $\tilde{A}(\mathbf{U})$ is the Fourier transform of the primary beam $A(\boldsymbol{\theta}, \nu)$. Under the assumption that $C_\ell(\nu)$ does not change much within the width of the function $|\tilde{A}(\mathbf{U} - \mathbf{U}')|^2$, the relation between $\Delta\tilde{T}_B(\mathbf{U})$ and the angular power spectrum $C_\ell(\nu)$ can be (Ali & Bharadwaj 2014) approximated as

$$\langle |\Delta\tilde{T}_B(\mathbf{U})|^2 \rangle = \left[\int d^2 \mathbf{U}' |\tilde{A}(\mathbf{U}')|^2 \right] C_\ell(\nu) \quad (16)$$

which allows us also to estimate $C_\ell(\nu)$ from $\Delta\tilde{T}_B(\mathbf{U}, \nu)$ or, equivalently, from the model visibilities $\mathbf{M}(\mathbf{U})$. Figure 5(c) shows the comparison between the angular power spectrum $C_\ell(\nu)$ estimated using equation (16) and the input model $C_\ell^M(\nu)$. The recovered angular power spectrum is in good agreement with the input model for $\ell \geq 100$, whereas the convolution with the primary beam (equation 15) is important at smaller ℓ . The fact that $|\mathbf{M}(\mathbf{U})|^2$ directly gives an estimate of $C_\ell(\nu)$ for most of the ℓ range shown in Figure 5(c) means that the correlation between the visibilities

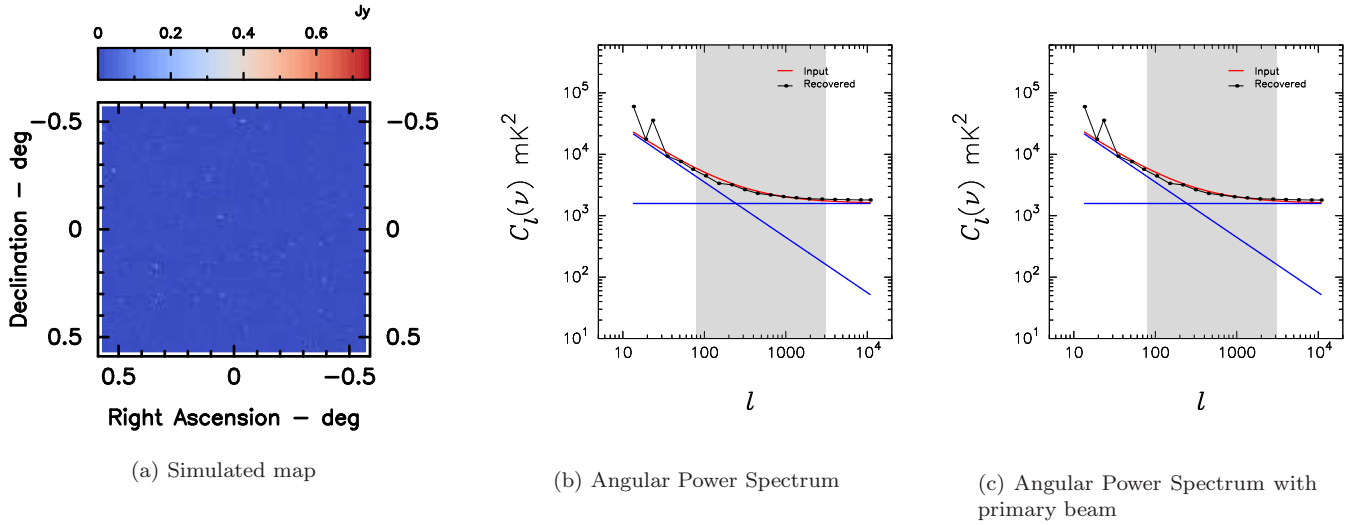


Figure 6. (colour online) (a) shows a zoomed in view of a single realization of the simulated brightness temperature map $\delta T(\theta, \nu)$ in (α, δ) coordinates for the nominal frequency of $\nu = 326.5$ MHz. In (b) the black points show the angular power spectrum recovered from the simulated map shown in (a), the input model angular power spectrum $C_\ell^M(\nu)$, is shown by the curve in red. The shaded region shows the multipole range $\ell_{\min} - \ell_{\max}$ accessible to OWFA. (c) shows the angular power spectrum recovered by applying equation (16) to the image obtained for a single realisation by multiplying the simulated map (a) with the primary beam pattern shown in Figure 4(b). The approximation is valid throughout the entire ℓ range, except at the smallest multipoles.

measured at OWFA can be used directly to estimate the angular power spectrum of the sky signal, an issue that we explore in detail later.

The values of the three parameters α , A_{150} and γ have been held constant in our simulations. In reality the spectral index α can vary along different lines of sight, and the amplitude A_{150} and γ is the index of the spatial power can have different values in different patches of the sky (e.g. La Porta et al. 2008). These variations will introduce additional angular and frequency structures as compared to the predictions of our simulations.

4.2 Extragalactic radio sources

The dominant emission from the 326.5-MHz sky at most of the angular scales of our interest is expected to be from the extragalactic point sources (Ali & Bharadwaj 2014). Wieringa (1991) has measured the source counts at 325 MHz with the WSRT down to ~ 4 mJy. More recently, Sirothia et al. (2009) have measured the source counts in the ELAIS N1 field at 325 MHz with the GMRT, the deepest till date. Ali & Bharadwaj (2014) have estimated that at most of the angular scales of P-II and at all scales of P-I, the extragalactic point source contribution is likely to dominate when observing at high galactic latitudes. The extragalactic radio source power spectrum has a flat Poisson part and a clustered part with a non-zero slope (Cress et al. 1996; Condon 2007; Owen & Morrison 2008; Vernstrom 2015).

Simulating extragalactic radio sources, most of which are unresolved at the resolution of OWFA, is more involved than the straightforward Fourier inversion of a power spectrum of the diffuse foreground. Details of the method used here can be found in González-Nuevo et al. (2005) but we summarize it here for completeness. Let \bar{n} be the mean num-

ber density of sources per pixel. Note that we have $\bar{n} \geq 1$ for a confusion limited map. We begin with a random Poisson field of mean source density \bar{n} , for which the density contrast is defined as $\delta(\theta) = [n(\theta) - \bar{n}]/\bar{n}$, and its Fourier transform is denoted using $\Delta(\mathbf{U})$. Let its angular power spectrum of $\delta(\theta)$ be denoted by C_ℓ^P , which can be calculated from $\Delta(\mathbf{U})$. We modify C_ℓ^P by the clustering angular power spectrum C_ℓ^{cl} : accordingly the Fourier transform of the density contrast is modified as

$$\Delta'(\mathbf{U}) = \Delta(\mathbf{U}) \sqrt{\frac{C_\ell^P + C_\ell^{cl}}{C_\ell^P}} \quad (17)$$

The modified density contrast spectrum $\Delta'(\mathbf{U})$ is reverse transformed to give the modified density contrast function $\delta'(\theta)$. Finally, the modified pixel source density is given by $n'(\theta) = \bar{n}[1 + \delta'(\theta)]$. The input power spectra for the Poisson part and the clustered part are respectively (from Ali & Bharadwaj 2014),

$$C_\ell^P = \left(\frac{\partial B}{\partial T}\right)^{-2} \int_0^{S_c} S^2 \frac{dN}{dS} dS \quad (18)$$

and

$$C_\ell^{cl} = 3.3 \times 10^{-5} \cdot \left(\frac{\partial B}{\partial T}\right)^{-2} \left[\int_0^{S_c} S^2 \frac{dN}{dS} dS \right] \left(\frac{1000}{\ell}\right)^\gamma \quad (19)$$

The integrals have been computed from a polynomial fit to the source counts from Wieringa (1991). The simulated map represents the true source distribution in the sky as no bright sources are assumed to have been subtracted, equivalent to an infinite cutoff flux. However, we impose a cutoff of 30 Jy in the numerical integration: this is a reasonably good approximation to an infinite cutoff flux, as the number of sources beyond ~ 3 Jy falls very sharply, and this behaviour is well captured by the polynomial approximation to the differential source counts. The clustered part

has a power law index of $\gamma = 0.9$ (Cress et al. 1996). The mean values are $C_{1000}^P = 1580 \text{ mK}^2$ and $C_{1000}^{cl} = 444 \text{ mK}^2$. We now populate the pixels with radio sources according to the observed differential source count relation, drawing from the distribution described by the polynomial obtained for the fit. The spectral indices for the point source fluxes have been assigned randomly, drawing from a Gaussian fit to the distribution centered at $\alpha = 0.7$ with a dispersion of $\sigma_\alpha = 0.25$ (Sirothia et al. 2009) and their channel-wise fluxes scaled accordingly. The angular resolution of these simulated maps ($\sim 1' \times 1'$) is equal to the 325-MHz WSRT resolution of Wieringa (1991), much finer than the OWFA resolution of $6'$. Figure 6(a) shows a single realization of the simulated brightness temperature map in $\delta T(\boldsymbol{\theta}, \nu)$ in (α, δ) coordinates. The angular power spectrum of the single random realization $C_\ell(\nu)$, shown in Figure 6(b), is seen to be in good agreement with the input model $C_\ell^M(\nu)$ except at the smallest multipoles. Figure 6(c) shows the comparison between the angular power spectrum $C_\ell(\nu)$ estimated using equation (16) and the input model $C_\ell^M(\nu)$.

The confusion limit for OWFA is 175 mJy (Ali & Bharadwaj 2014); however, we do not propose to identify and subtract sources from the one-dimensional images made using the OWFA itself. Instead, a model for the sky obtained from deep GMRT imaging could, for example, be used to subtract the contribution to the visibility from the extragalactic radio sources. Alternatively, the model visibilities upto 18 mJy (the 5σ limit) could just as well be obtained from the shallower Westerbork Northern Sky Survey (WENSS; Rengelink et al. 1997).

5 POWER SPECTRUM ESTIMATION

5.1 The two-visibility correlation as the MAPS estimator

The issue here is to use the measured OWFA visibilities $\mathcal{V}(\mathbf{U}_n)$ to estimate the statistics of the background sky signal. Before discussing the method of analysis, it is important to note that the baseline \mathbf{U}_n corresponding to a fixed antenna separation \mathbf{d}_n scales as $\mathbf{U}_n = \nu \mathbf{d}_n/c$ (equation 8) with ν varying across the observing band. This renders it difficult to use \mathbf{U}_n and ν_i as independent parameters to label the visibilities $\mathcal{V}(\mathbf{U}_n)$ that will be measured at OWFA. For the purpose of analyzing the data we adopt the notation where $\mathbf{U}_n = \nu_c \mathbf{d}_n/c$ which does not vary with frequency but is fixed at $\nu_c = 326.5 \text{ MHz}$. In this notation we may interpret \mathbf{U}_n and ν_i as independent parameters that label the visibilities $\mathcal{V}(\mathbf{U}_n, \nu_i)$.

The proposed method of analysis is here applied to simulated data which only contains the foreground components. As described in the previous section, the foregrounds all have simple power law frequency dependence in the models which we have implemented here. The telescope's chromatic response (equations 6 and 8), however, introduces additional frequency dependence which we have attempted to capture in the subsequent analysis.

The two point statistics or, equivalently the power spectrum of the sky signal, is entirely contained in the two visibility correlation

$$\mathbf{S}_2(\mathbf{U}_n, \nu_i; \mathbf{U}_m, \nu_j) \equiv \langle \mathcal{V}(\mathbf{U}_n, \nu_i) \mathcal{V}^*(\mathbf{U}_m, \nu_j) \rangle. \quad (20)$$

where the angular brackets denote an ensemble average over different random realisations of the sky signal.

In addition to the self-correlation ($n = m$), the signal in the adjacent baseline pairs ($n = m \pm 1$) are correlated (see Figure 4(c) and Ali & Bharadwaj 2014). Further, the correlation is approximately a factor of four smaller compared to the self correlation if we consider two adjacent baselines (Bharadwaj et al. 2015). For the present analysis we consider only the self-correlation, and we use the notation

$$\mathbf{S}_2(\mathbf{U}_n, \nu_i, \nu_j) \equiv \langle \mathcal{V}(\mathbf{U}_n, \nu_i) \mathcal{V}^*(\mathbf{U}_n, \nu_j) \rangle. \quad (21)$$

The relation between \mathbf{S}_2 and the power spectrum $P(\mathbf{k})$ of HI is well understood (Bharadwaj & Sethi 2001; Bharadwaj & Ali 2005; Ali & Bharadwaj 2014) and we do not consider it here.

The multi-frequency angular power spectrum $C_\ell(\nu_i, \nu_j)$ (MAPS; Datta et al. 2007) which is defined through

$$\langle \Delta \tilde{T}(\mathbf{U}, \nu_i) \Delta \tilde{T}_B^*(\mathbf{U}', \nu_j) \rangle = \delta_D^2(\mathbf{U} - \mathbf{U}') C_\ell(\nu_i, \nu_j) \quad (22)$$

provides an useful tool to jointly characterize the angular and frequency dependence of the statistical properties of the sky signal. Here $\delta_D^2(\mathbf{U} - \mathbf{U}')$ is the 2D Dirac delta function and we have $\ell = 2\pi|\mathbf{U}|$ in the flat sky approximation.

The model visibilities in equation 5 are related to the brightness temperature fluctuations $\Delta \tilde{T}(\mathbf{U}, \nu)$ as

$$\mathbf{M}(\mathbf{U}_n, \nu) = \left(\frac{\partial B}{\partial T} \right)_\nu \int d^2 \mathbf{U} \tilde{A}(\mathbf{U}_n(\nu/\nu_c) - \mathbf{U}, \nu) \Delta \tilde{T}(\mathbf{U}, \nu) \quad (23)$$

where $\left(\frac{\partial B}{\partial T} \right)_\nu$ is the conversion factor from brightness temperature to specific intensity, and we have introduced a factor (ν/ν_c) in the argument of \tilde{A} to account for the fact that \mathbf{U}_n is defined at ν_c . For the present analysis we assume that the visibilities are perfectly calibrated and altogether ignore the noise contribution. This leads to

$$\mathbf{S}_2(\mathbf{U}_n, \nu_i, \nu_j) = \left(\frac{\partial B}{\partial T} \right)_{\nu_i} \left(\frac{\partial B}{\partial T} \right)_{\nu_j} \int d^2 \mathbf{U} \times \quad (24)$$

$$\tilde{A}(\mathbf{U}_n(\nu_i/\nu_c) - \mathbf{U}, \nu_i) \tilde{A}^*(\mathbf{U}_n(\nu_j/\nu_c) - \mathbf{U}, \nu_j) C_{2\pi \mathbf{U}}(\nu_i, \nu_j)$$

which relates the visibility correlation to the multi-frequency angular power spectrum (MAPS). Note that it is possible to estimate the visibility correlation $\mathbf{S}_2(\mathbf{U}_n, \nu_i, \nu_j)$ directly from the measured visibilities, whereas $C_\ell(\nu_i, \nu_j)$ quantifies the intrinsic sky signal independent of any telescope. Equation (24) allows us to relate the statistics of the measured visibilities to the intrinsic statistics of the sky signal. We see that the telescope appears through a convolution in equation (24). It is, in principle, possible to determine $C_\ell(\nu_i, \nu_j)$ from the measured $\mathbf{S}_2(\mathbf{U}_n, \nu_i, \nu_j)$ by deconvolving the effect of the telescope's primary beam \tilde{A} , and we interchangeably refer to $\mathbf{S}_2(\mathbf{U}_n, \nu_i, \nu_j)$ as the visibility correlation or the MAPS estimator.

We now consider the restricted situation where $\nu_i = \nu_j$, and discuss how it is possible to use the measured $\mathbf{S}_2(\mathbf{U}_n, \nu_i, \nu_j)$ to estimate $C_\ell(\nu) \equiv C_\ell(\nu_i, \nu_i)$. We have already seen in equation (14) that for a large part of the ℓ range probed by OWFA it is possible to approximate the convolution in equation (24) by a multiplicative factor. This permits us to approximate $\mathbf{S}_2(\mathbf{U}_n, \nu_i, \nu_j)$ as

$$\mathbf{S}_2(\mathbf{U}_n, \nu, \nu) = K_\nu C_{\ell_n}(\nu) \quad (25)$$

where $\ell_n = 2\pi|\mathbf{U}_n|$ and K_ν is defined as

$$K_\nu = \left(\frac{\partial B}{\partial T} \right)_\nu^2 \int d^2 \mathbf{U}' |\tilde{A}(\mathbf{U}')|^2, \quad (26)$$

which is uniquely determined for a known primary beam. We can use equation (25) to estimate $C_\ell(\nu)$ from the measured visibility correlation.

Considering a fixed baseline \mathbf{U}_n , the visibility correlation $\mathbf{S}_2(\mathbf{U}_n, \nu_i, \nu_j)$ is (equation 24) a real valued symmetric matrix of dimensions $N_c \times N_c$ where N_c is the number of frequency channels. Observations will yield such a matrix for every available unique baseline \mathbf{U}_n . For OWFA (Table 1) we have a limited number of such baselines all of which are aligned with the N-S direction, allowing us to label the baselines with just numbers U_n instead of vectors \mathbf{U}_n . Earlier studies (e.g. Bharadwaj & Sethi 2001; Ali & Bharadwaj 2014) show that the HI signal contribution to $\mathbf{S}_2(\mathbf{U}_n, \nu_i, \nu_j)$ can be modelled as $\mathbf{S}_2(\mathbf{U}_n, \Delta\nu_{ij})$ which depends only on the frequency separation $\Delta\nu_{ij} = |\nu_i - \nu_j|$. It is further predicted that $\mathbf{S}_2(\mathbf{U}_n, \Delta\nu_{ij})$ has a maximum value at $\Delta\nu_{ij} = 0$, and decorrelates rapidly as the separation $\Delta\nu_{ij}$ increases, with a value close to zero for large values of $\Delta\nu_{ij}$ (see e.g. Chatterjee et al. 2017, for result from simulation). $\mathbf{S}_2(\mathbf{U}_n, \Delta\nu)$ is predicted to be close to zero for $\Delta\nu_{ij} \geq 1$ MHz on nearly all of the baselines that will be probed by P-I of OWFA (Ali & Bharadwaj 2014). This essentially implies that the HI signal is mainly localized near the diagonal elements of the visibility correlation matrix $\mathbf{S}_2(\mathbf{U}_n, \nu_i, \nu_j)$, the elements which are located far away from the diagonal are expected to not have much of the HI signal. It is therefore reasonably safe to assume that the matrix elements located at a distance from the diagonal are entirely dominated by the foregrounds with a negligible HI contribution.

In the current work we present preliminary results where we explore the frequency dependence of $\mathbf{S}_2(\mathbf{U}_n, \nu_i, \nu_j)$ in order to assess the contribution to such effects from the instrument itself. We note that an earlier version of the visibility correlation-based estimator presented here has been applied to measure the foreground C_ℓ in 150 MHz GMRT observations (Ali et al. 2008; Ghosh et al. 2012), and also for foreground removal in 610 MHz GMRT observations (Ghosh et al. 2011a,b).

5.2 Computing the estimator

In practice, we would calibrate the observed visibilities making use of the redundant spacings (e.g. Wieringa 1992; Liu et al. 2010; Marthi & Chengalur 2014). In this simulation we directly use the model visibilities, equivalent to the observed visibilities having been already calibrated. For a baseline \mathbf{U}_n and a frequency channel ν_i , let there be N_n distinct measurements of the visibility $\mathcal{V}^{(a)}(\mathbf{U}_n, \nu_i)$ labelled using $a = 1, 2, \dots, N_n$. Note that each redundant spacing as well as each time sample is a distinct measurement of the visibility³. The N_n distinct measurements all measure the same Fourier mode on the sky, given by the model visibilities $\mathcal{M}(\mathbf{U}_n, \nu_i)$. The system noise contribution $\mathcal{N}^a(\mathbf{U}_n, \nu_i)$

³ This is true only when the telescope tracks the sky continuously. We do not consider the drift-scan mode of observing in this article.

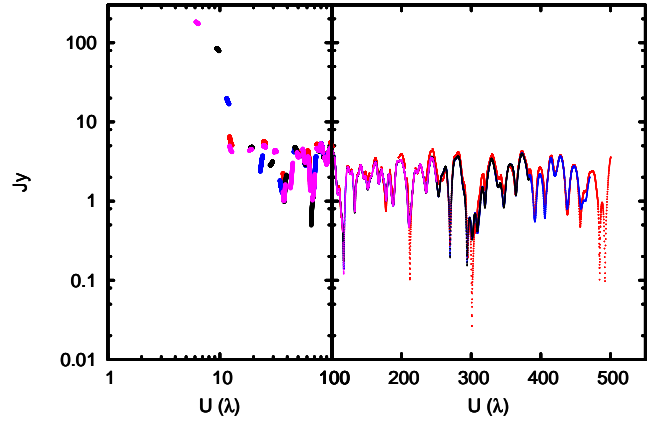


Figure 7. (colour online) The red, blue, black and magenta colours code respectively the declinations 0° , 20° , 40° and 60° . This figure shows the magnitude of the model visibilities for a single realization of the sky, the emission from the larger scales being picked up by the shortened baselines at increasing declination.

(equation 11), however, is different in each of these measurements: its contribution to each visibility measurement is an independent Gaussian random variable, and the different visibility measurements can be added coherently (after calibration) to improve the signal-to-noise ratio; this is a unique feature of OWFA. Therefore, the sum

$$\bar{\mathcal{V}}(\mathbf{U}_n, \nu_i) = \frac{1}{N_n} \sum_{a=1}^{N_n} \mathcal{V}^{(a)}(\mathbf{U}_n, \nu_i) \quad (27)$$

shows a baseline-dependent $1/\sqrt{N_n}$ noise behaviour.

We can, in principle, use $\bar{\mathcal{V}}(\mathbf{U}_n, \nu_i)\bar{\mathcal{V}}^*(\mathbf{U}_n, \nu_j)$ to estimate the visibility correlation $\mathbf{S}_2(\mathbf{U}_n, \nu_i, \nu_j)$. The correlation $\mathbf{S}_2(\mathbf{U}_n, \nu_i, \nu_j)$, however, will pick up an extra, positive, noise bias $\sum_{a=1}^{N_n} |\mathcal{N}^a(\mathbf{U}_n, \nu_i)|^2 / (N_n)^2$ arising from the correlation of a visibility with itself. It is possible to avoid this noise bias (e.g. Begum et al. 2006; Choudhuri et al. 2016b) by subtracting out the self correlation

$$\bar{\mathcal{V}}_2(\mathbf{U}_n, \nu_i) = \frac{1}{N_n} \sum_{a=1}^{N_n} |\mathcal{V}^{(a)}(\mathbf{U}_n, \nu_i)|^2. \quad (28)$$

We hence define our estimator \mathbf{S}_2 as

$$\mathbf{S}_2(\mathbf{U}_n, \nu_i, \nu_j) = \frac{N_n^2 \bar{\mathcal{V}}(\mathbf{U}_n, \nu_i)\bar{\mathcal{V}}^*(\mathbf{U}_n, \nu_j) - \delta_{ij} N_n \bar{\mathcal{V}}_2(\mathbf{U}_n, \nu_i)}{N_n^2 - \delta_{ij} N_n} \quad (29)$$

which is free from the noise bias arising from the correlation of a measured visibility with itself.

6 RESULTS

6.1 Visibilities

The model visibilities are computed for a sky model that consists of the sum of a realization of the diffuse foreground and the extragalactic radio sources. The full U -range of the OWFA is $\sim 0 - 500\lambda$ at $\delta_0 = 0^\circ$. However, for fields at high declinations, the range of U is compressed by the factor $\cos \delta_0$, where δ_0 is the declination of the centre of the field. The model visibilities for a single realization of the sky that

includes both the diffuse emission and extragalactic radio sources for four different declinations are shown in Figure 7. The higher declinations allow for a compressed range of U , thereby accessing more of the extended emission at $U < 100$. However, the sensitivity reduces equally by $\cos \delta_0$ due to the smaller projected aperture.

6.2 The Foreground Power Spectrum

In this section we provide results for the visibility correlation MAPS estimator. As a verification step, we start with a noise-free simulation, and use the model visibilities directly: the assumption of perfect calibration and absence of ionospheric effects and RFI is implicit. The MAPS estimator returns a matrix of the visibility correlation $\mathbf{S}_2(\mathbf{U}_n, \nu_i, \nu_j)$ as a function of the pair of frequencies at which it is computed. Each panel (left to right) in Figure 8 is the matrix (read top left to bottom right) $\mathbf{S}_2(\mathbf{U}_n, \nu_i, \nu_j)$ for the OWFA baselines $n = 1, 16$ and 32 respectively.

This observation is simulated for a declination of $\delta = 0^\circ$ and includes the diffuse Galactic emission as well as the point source contribution. The three panels of Figure 8 (left to right), have different (decreasing) foreground amplitudes. As discussed in Figure 9 of Ali & Bharadwaj (2014), the diffuse Galactic emission is the dominant component at short-baseline as apparent in the left panel of the Figure 8. The clustered point source component dominates at small angular scales or the larger baselines ($U \lesssim 300$) which can be seen in the middle panel. The foreground amplitude right panel where $U \simeq 400$, is dominated by the Poisson contribution. The foregrounds appear to be quite smooth in the $\nu_i - \nu_j$ plane, suggesting that this could possibly be used to separate the H I signal, which has a different signature in \mathbf{S}_2 , from the foregrounds. Note that the foregrounds exhibit a particularly smooth frequency dependence at the smallest baseline (left panel), and the frequency variations become progressively more rapid as we move to larger baselines. Much of the frequency structure seen in the central and right panels is clearly not a function of the frequency separation $\Delta\nu = |\nu_i - \nu_j|$ alone, and these structures are visible even at large $\Delta\nu$, or away from the diagonal. This distinction between the foregrounds and the H I signal leads to separable features between the foregrounds and H I in the k -space.

We next use the diagonal elements $\mathbf{S}_2(\mathbf{U}_n, \nu_i, \nu_i)$ of the measured MAPS to estimate the angular power spectrum $C_{\ell_n}(\nu_i, \nu_j)$ of the sky signal using equation (25). Figure 9(a) shows $C_{\ell}(\nu)$ recovered from two simulated realisations of the diffuse Galactic foregrounds. The solid line is the input analytical angular power spectrum and the points represent the recovered angular power spectrum for a single realisation. Similarly, Figure 9(b) shows the recovered angular power spectrum for the extragalactic point sources, where the solid line is the input angular power spectrum, which is the sum of the Poisson and the clustered contributions. We see that the recovered angular power spectrum is in excellent agreement with the input model for the entire ℓ range shown in the figure. In both cases, the dashed line represents the model used to obtain a random realization, and serve only as a visual aid. We reiterate that the results are shown here for a noiseless simulation. The MAPS estimator, in addition, is unbiased as it avoids the self-noise contribution through

equation (29). In a future article, we will explore applying the tapered gridded estimator (TGE; Choudhuri et al. 2014), tailoring it suitably for OWFA.

7 DISCUSSION

We will now discuss some properties of the estimator in the context of the OWFA experiment, including limitations posed by the instrument systematics. We will look at the following aspects in succession:

- The estimator shows predictable spectral behaviour and introduces no spectral anomalies.
- The chromatic primary beam and the chromatic response function of the interferometer dominate well over the chromaticity of the measured sky signal.
- Contribution from sources in the sidelobes manifest as spectral signatures in the estimator.
- The error on the estimator can be derived from the data.

7.1 Spectral behaviour

The MAPS estimator has a fully tractable spectral response. Since it is possible to analytically derive the spectral response of the estimator, we can ascertain through simulations that the estimator introduces no unaccounted features in the spectrum. This means that, in principle, it is possible to model out the instrument-induced spectral features in the estimator.

It has been shown that the angular power spectrum $C_{\ell}(\nu)$ and the MAPS estimator $\mathbf{S}_2(\mathbf{U}, \nu_i, \nu_j)$ are related by equation (24), where for our assumed sinc-squared primary beam,

$$\tilde{A}(\mathbf{U}, \nu) = \frac{\lambda^2}{bd} \Lambda\left(\frac{u\lambda}{d}\right) \Lambda\left(\frac{v\lambda}{b}\right) \quad (30)$$

is the Fourier transform of the primary beam power pattern, $\mathbf{U} = (u, v)$ and $\Lambda(x)$ is the triangular function defined as

$$\Lambda(x) = 1 - |x| \text{ for } |x| < 1, \text{ and } \Lambda(x) = 0 \text{ for } |x| \geq 1. \quad (31)$$

Given that $\ell = 2\pi U$ where $U = d/\lambda$, we may write

$$C_{\ell} \propto \left(\frac{\lambda}{d}\right)^{\gamma} \quad (32)$$

It then follows that for the visibility correlation of the diffuse foreground signal alone,

$$\mathbf{S}_2 \propto \nu^{2(1-\alpha)-\gamma} \quad (33)$$

considering all the spectral contributions, namely the intrinsic spectral index α , the power law index dependence on frequency through ℓ , and the Fourier transform of the primary beam power pattern.

Restating that the spectral response of the estimator is fully tractable, we illustrate this for a simple case where $\alpha = 2.32$ and $\gamma = 2.54$. The \mathbf{S}_2 matrix is obtained for 1000 independent but noiseless realisations of the diffuse Galactic foreground and the mean and the 1σ error bars of these diagonals are computed. The mean and the error bars are then individually normalised at $\nu = 326.5$ MHz; the normalised mean and error bar curves can be represented as $\|\mathbf{S}_2(\nu)\|$

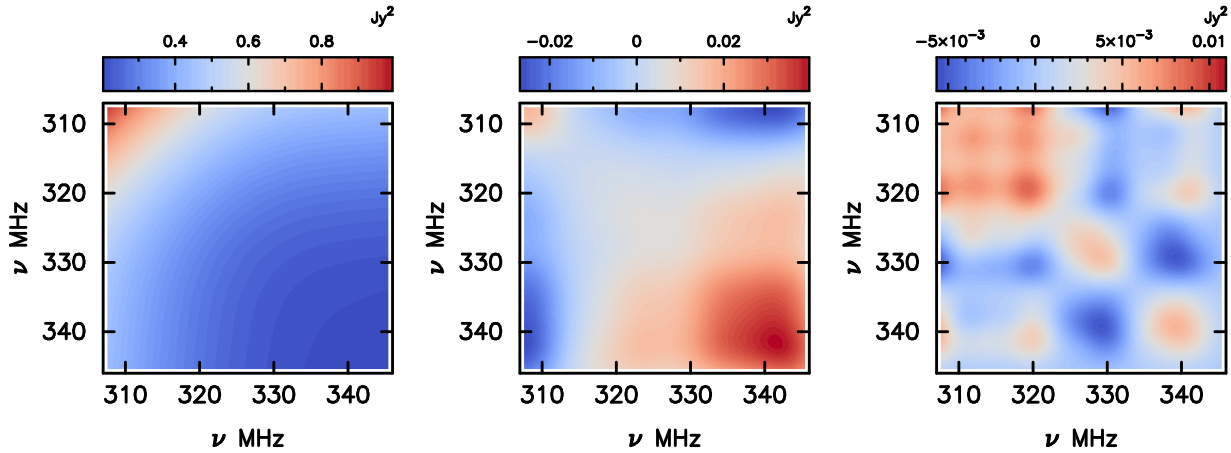


Figure 8. (colour online) The MAPS estimator $\mathbf{S}_2(U_n, \nu_i, \nu_j)$ for a single realization of the sky, for simulated observations at $\delta = 0^\circ$ for OWFA baselines $n = 1, 16$ and 32 increasing from left to right panel. The diagonal in each matrix is the locus of $\Delta\nu = 0$, and any point on the diagonal through the MAPS for the baselines stacked in sequence is a proxy for $C_\ell(\Delta\nu = 0)$. In addition to the shorter baselines having more power, the longer baselines exhibit enhanced spectral structure, both in line with our understanding. See text for details

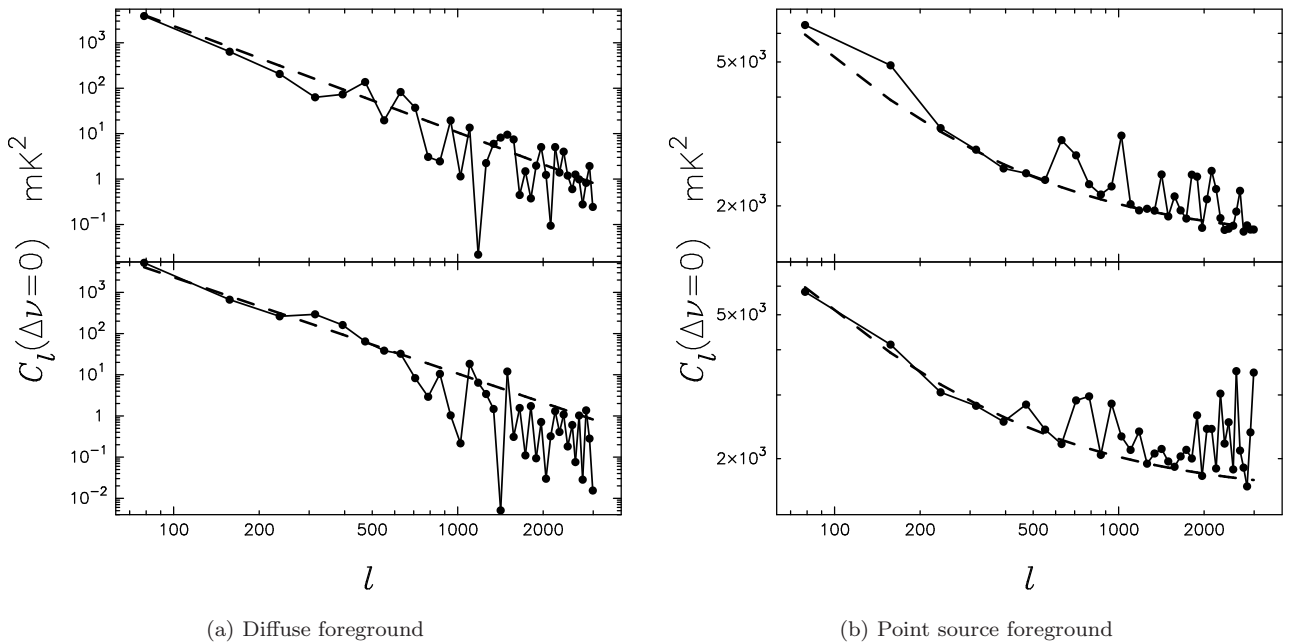


Figure 9. (a) The angular power spectrum of the diffuse Galactic emission: input model shown with the solid line and the power spectrum recovered through the estimator with points, for two random realisations. (b) The angular power spectrum of extra-galactic point sources. In both the plots, the dashed line represents the analytical expression for the power spectra used to obtain the random realisations, shown here only to compare the random realisations against. The results are at the frequency $\nu_c = 326.5$ MHz.

and $\|\Delta\mathbf{S}_2(\nu)\|$. Figure 10 shows the normalised mean of the diagonals as filled black circles. These have been sampled at every tenth channel so that they are seen clearly in the plot. The shaded region represents the bounds of the 1σ error on the mean of the foreground realisations. The curves in red are the normalised (at 326.5 MHz) $\mathbf{S}_2(\nu)$ curves for two different realisations. The black curve is the mean of all the realisations and it agrees remarkably well with the expression $\left(\frac{\nu}{\nu_0}\right)^{2(1-\alpha)-\gamma}$. We make a few points to enable a

clear interpretation of Figure 10. Firstly, the error bounds on the analytical curve arise from the unit variance complex random variable $(x + iy)/\sqrt{2}$ in equation (14). Therefore, it shows the standard deviation of the random realisations and not the estimator. The standard deviation computed from the realisations is indeed unity, which is easy to see at $\nu_c = 326.5$ MHz. In addition, the red curves show just two of such random realisations, and there is visibly more spectral structure on the longer baselines. As a result of which,

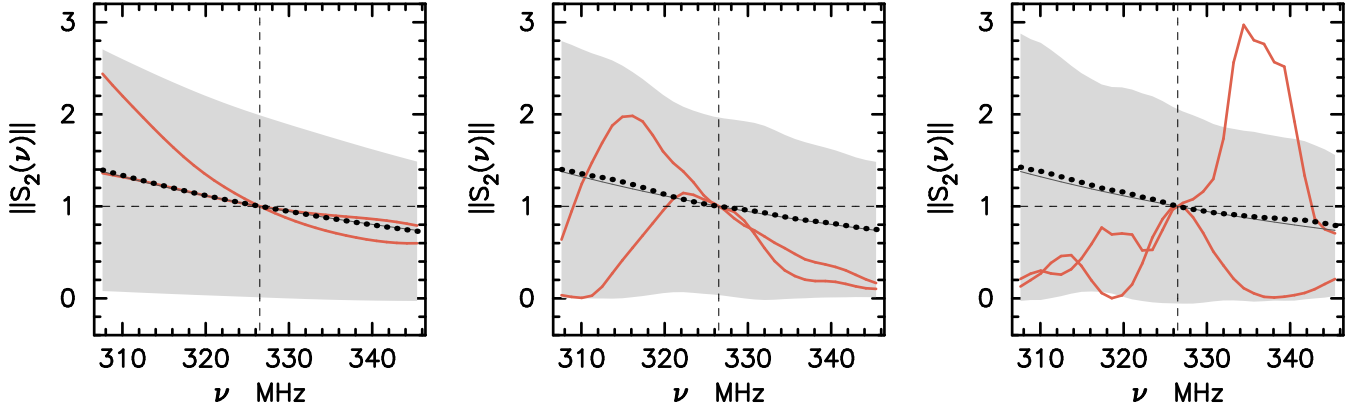


Figure 10. (colour online) The normalised MAPS estimator $\|\mathbf{S}_2(U, \nu)\|$ is shown left to right, top to bottom, for baselines 4, 21 and 31. The red curves relate to two different realisations of the diffuse Galactic synchrotron foreground from a total of 1000. The estimated mean is given by the filled circles and the solid black line is the analytically computed curve given by $(\nu/\nu_0)^{(2-2\alpha-\gamma)}$. The simulation is over 39 MHz split into 312 channels, but only a sampled version of the estimated mean (filled circles) is shown for clarity. The shaded region represents the 1σ error bound on the random foreground realisations.

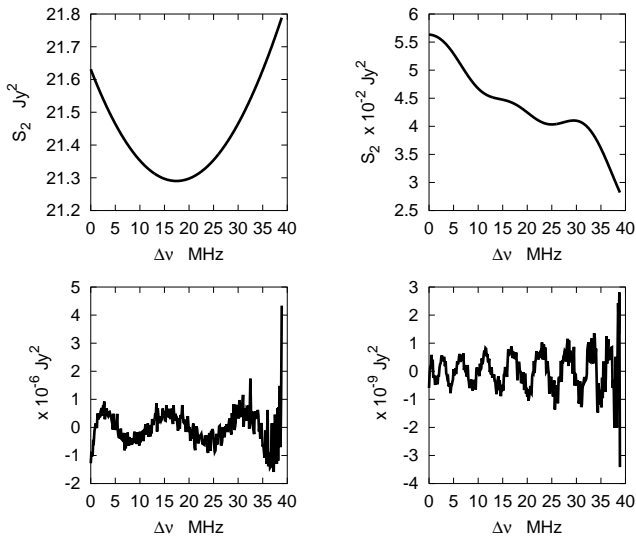


Figure 11. The $\mathbf{S}_2(\Delta\nu)$ curves for two baselines U_2 and U_{17} are shown in the top left and right panels respectively. The residual after fitting polynomials are shown in the bottom panels, indicating the contribution from sources in the sidelobes.

lastly, the match is not visibly exact for the longer baseline between the analytical curve and the estimated mean data points. A progressively larger number of realisations would have to be averaged for the match to appear exact on the longer baselines. In addition, the shaded bounds allow for a comparison of these two realisations with the error on the mean, clearly showing more variance on the longer baselines.

A source away from the phase centre leaves oscillatory features in the MAPS estimator, and the frequency of the oscillation depends on the location of the source m as well on the baseline nd . It is interesting to note that $\Delta\nu/\nu_0$ is of the order of 12% (~ 40 MHz/327 MHz) for OWFA. The argument can be generalised to include many point sources, and by extension to the diffuse foregrounds as well. The sum total contribution from all emission within the field of view superimpose with a range of phases that tend to

partly cancel out. But residual features remain imprinted on the innocuous-looking smooth spectra. Figure 11 shows the \mathbf{S}_2 for the same realisation of diffuse and point source foregrounds used to obtain the plots in Figure 8, but computed as a function of $\Delta\nu$ by averaging along the diagonals of the \mathbf{S}_2 matrix for two example baselines. Although the foregrounds are non-stationary as discussed in Section 5.2, it is instructive to cast the estimator in the familiar form as a function of $\Delta\nu$ for this exercise. The apparently smooth curves in the top panels can be fitted by low-order polynomials successively. The residual contamination can still be seen in the bottom panels. The frequency of the oscillatory pattern is higher as expected for longer baselines. It must be noted that the amplitude of the residual oscillatory features is about 7 orders smaller than the visibility correlation \mathbf{S}_2 . These features are still about 1-2 orders above the amplitude of the expected H I visibility correlation (see Ali & Bharadwaj 2014; Chatterjee et al. 2017). At this level, these dominant residual features preclude detecting the H I signal in the $\Delta\nu$ space.

These undesirable oscillatory features can be suppressed by restricting the total FoV. This can be achieved by tapering the primary beam with a weighting function, typically a Gaussian window function. However, this is possible only in the uv -plane post-correlation, through a 2D convolution. Beam tapering in uv has been shown to be quite effective for the GMRT (Ghosh et al. 2011b). The tapered-gridded estimator has been shown to be equally effective for simulated GMRT data (Choudhuri et al. 2014, 2016a).

The function $\mathbf{S}_2(\mathbf{U}, \nu_1 - \nu_2)$ behaves smoothly away from and normal to the principal diagonal. Since this cut normal to the diagonal represents $\mathbf{S}_2(\mathbf{U}, \Delta\nu)$, the MAPS estimator matrix \mathbf{S}_2 naturally encodes the decorrelation of the foreground as well as the sky signal.

7.2 Sources in the sidelobes and instrument chromaticity

The effects of sources at large angular distances from the pointing centre coupling in through the primary beam is

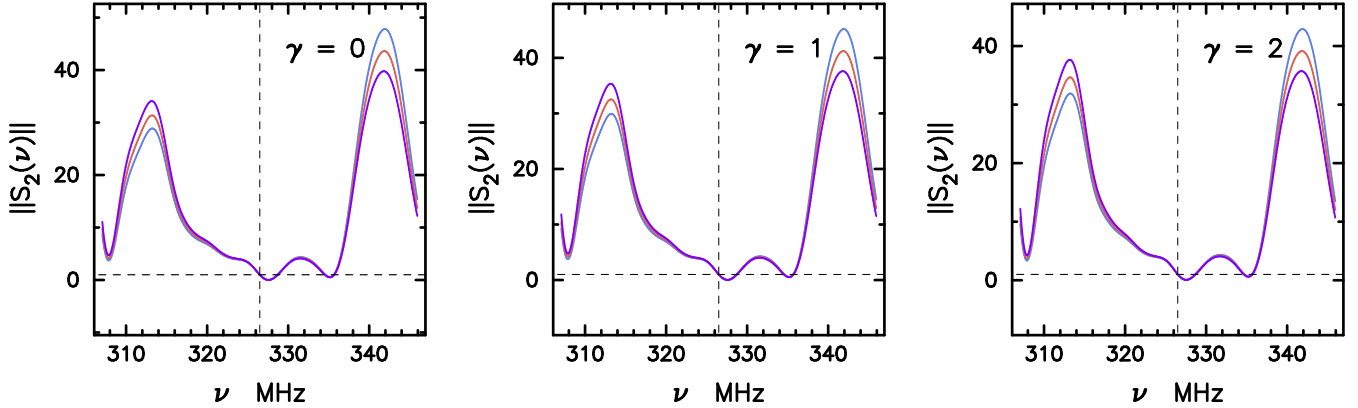


Figure 12. (colour online) The estimator $\mathbf{S}_2(\nu)$ for different values of α and γ are shown here for the longest baseline $|U| = 475.0$. Each plot has three curves; one each for $\alpha = 0.0, 1.0, 2.0$, shown by the colours blue, red and purple respectively. The values have been normalised to $\mathbf{S}_2(\nu)$ at $\nu = 326.5$ MHz. The normalized curves look very similar between widely different values for α and γ , implying that these estimates are dominated not by α and γ , but by the instrument response. The dashed lines mark $\nu_c = 326.5$ MHz and $\|\mathbf{S}_2(\nu_c)\| = 1$.

well-known (see e.g. [Datta et al. 2010](#); [Vedantham et al. 2012](#); [Pober et al. 2013b](#); [Thyagarajan et al. 2015a,b](#); [Pober et al. 2016](#)). Consider a single point source at the coordinates $\boldsymbol{\theta} = (l, m)$. Let us also assume that the pointing of observation is $(\alpha_0 = 0, \delta_0 = 0)$ without loss of generality. For the n^{th} baseline in the linear array, we note that at frequency $\nu = c/\lambda$,

$$U_n = nU_1 = n \frac{d}{\lambda} = n \frac{d}{\lambda_0} \frac{\lambda_0}{\lambda} \quad (34)$$

The visibility, obtained as a Fourier sum in the simulation and given in equation 10, simplifies to

$$M(\mathbf{U}, \nu) = \sum_{\boldsymbol{\theta}} I(\boldsymbol{\theta}, \nu) A(\boldsymbol{\theta}, \nu) e^{-i2\pi m \frac{nd}{\lambda_0} \frac{\lambda_0}{\lambda}} \quad (35)$$

Since $\mathcal{V}(\mathbf{U}, \nu)$ represents an estimate of $M(\mathbf{U})$, the two-visibility correlation at (ν_i, ν_j) for this baseline becomes

$$\mathbf{S}_2(U_n, \nu_i, \nu_j) \sim |I(\boldsymbol{\theta}, \nu_0)|^2 |A(\boldsymbol{\theta}, \nu_0)|^2 e^{-i2\pi m \left(\frac{nd}{\lambda_0}\right) \left(\frac{\nu_i - \nu_j}{\nu_0}\right)} \quad (36)$$

assuming that the approximations

$$|I(\boldsymbol{\theta}, \nu_0)|^2 = I(\boldsymbol{\theta}, \nu_i) I^*(\boldsymbol{\theta}, \nu_j) \quad (37)$$

and

$$|A(\boldsymbol{\theta}, \nu_0)|^2 = A(\boldsymbol{\theta}, \nu_i) A^*(\boldsymbol{\theta}, \nu_j) \quad (38)$$

are reasonable, but in general not strictly true.

The intrinsic frequency dependence of the sky signal can be disentangled from the chromatic instrument response by varying α and γ over a range of values. We observe the resulting spectral behaviour \mathbf{S}_2 for a single Gaussian realization of the diffuse foreground. Figure 12 shows $\mathbf{S}_2(\Delta\nu = 0)$ normalised to its value at $\nu = 326.5$ MHz, for the longest baseline, where α is allowed to take three different values: 0.0, 1.0 and 2.0 (the three curves in each panel) for each $\gamma = 0, 1, 2$. The spatial index γ exerts a spectral dependence through $\nu^{-\gamma}$, and the spectral index α through $\nu^{2(\alpha-2)}$. Therefore for $\gamma = 0$ and $\alpha = 2$ (spectral index in temperature units), all the spectral behaviour that manifests

in the curve is indeed being caused by (a) the baselines U changing with frequency and (b) the primary beam shrinking with increasing frequency. The strikingly similar curves for different values of α and γ point to their effect being sub-dominant. Therefore, the bulk of the spectral trend of \mathbf{S}_2 in a single foreground realisation comes from the chromatic response of the instrument (see also [Vedantham et al. 2012](#); [Thyagarajan et al. 2013](#)).

7.3 Error on the estimator

Having studied the visibility correlation estimator through noise-free simulations, we could now turn our attention to the effects of noise. The estimator \mathbf{S}_2 has the dimensions of variance. For the error on \mathbf{S}_2 we are hence interested in the variance of the variance. In the simulations described above, the visibility correlation matrix \mathbf{S}_2 is computed at every one-second interval. For an N -second observation, therefore, N such matrices are available for each baseline, from which the mean matrix and the RMS matrix for each baseline can be computed.

The estimator \mathbf{S}_2 and the error matrix $\Delta\mathbf{S}_2$ are computed now for a single realisation of the Galactic diffuse foreground, with the system temperature of 150 K ([Selvanayagam et al. 1993](#)) and a 60-second observation. This is equivalent to deriving the error bars from as many independent realisations (60) of the noise, given a single realisation of the foreground. Figure 13 shows the recovered power spectrum by sampling through the mean and RMS cubes, \mathbf{S}_2 and $\Delta\mathbf{S}_2$, at the same (ν_i, ν_j) co-ordinates: the power spectrum is obtained from the mean \mathbf{S}_2 matrix and the error bars from the RMS $\Delta\mathbf{S}_2$ matrix. Figure 13(a) shows the “self” power spectrum with the error bars where $\nu_i = \nu_j = 326.44$ MHz, and Figure 13(b) shows the “cross” power spectrum with error bars, at $\nu_i = 342.19$ MHz and $\nu_j = 326.94$ MHz. The dashed straight line through the plots is not a fit, but it is the input analytical power spectrum used for simulating the diffuse Galactic foreground. The U values on the x -axis are computed at the central frequency 326.5 MHz, as there is no other meaningful way to represent

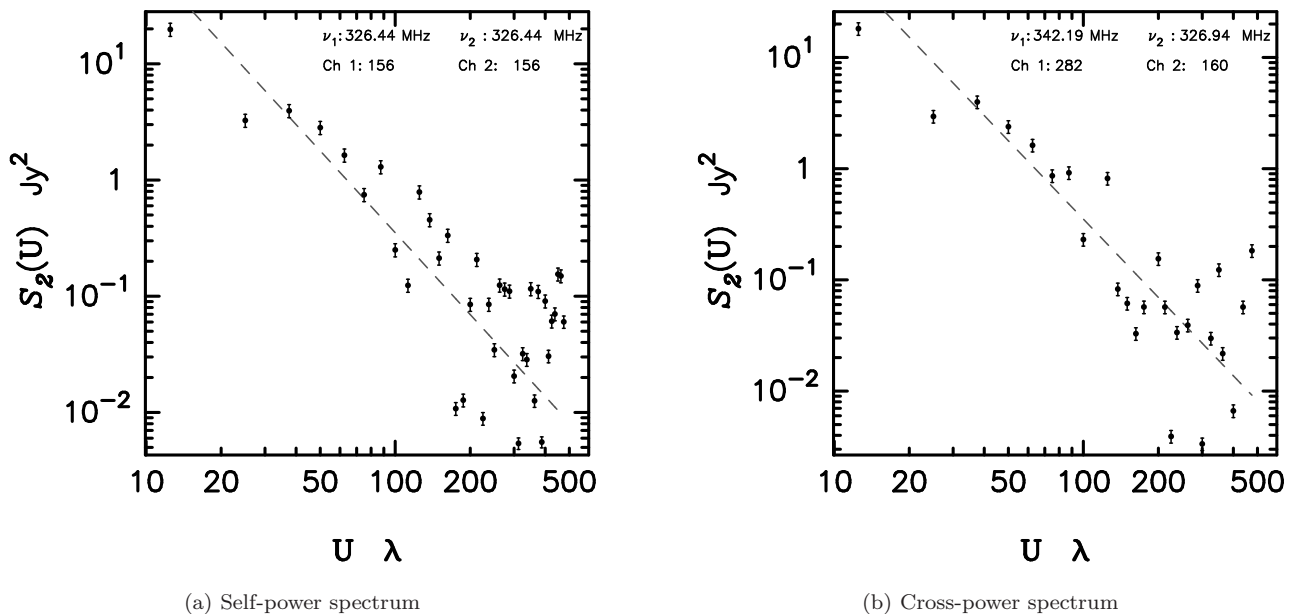


Figure 13. The panels (a) and (b) respectively show the “self-power spectrum” and “cross-power spectrum” at different values of (ν_i, ν_j) by sampling through the \mathbf{S}_2 cube. The error bars, drawn from the same co-ordinates of the RMS cube, correspond to 60 seconds of integration with a system temperature of $T_{\text{sys}} = 150$ K. The dashed straight line is the input angular power spectrum of the Galactic diffuse synchrotron foreground. The scatter in the estimated power spectrum is due to the stochastic nature of a single realization of the foreground.

U at a pair of frequencies (ν_i, ν_j) at which these spectra have been extracted. Figure 13 is an important result purely from the perspective of foregrounds: a 60-second integration has resulted in a 10σ detection of the diffuse Galactic foregrounds, under the implicit assumption that the point source foregrounds have been modelled out, or are sub-dominant as would be the case for the short baselines of OWFA. This is a very optimistic scenario if we are interested in the statistics of the diffuse foregrounds.

8 SUMMARY

In this paper we have briefly described the upcoming Ooty Wide Field Array interferometer, one of whose goals is to detect the large scale structure in redshifted 21-cm emission from $z \sim 3.35$. A detailed simulation of the instrument and the foregrounds has been carried out. The simulations incorporate a fully chromatic instrument model and hence lead to conservative estimates for the expected systematics. We have recast the visibility correlation estimator, previously applied to GMRT observations, for OWFA. We find that the foregrounds manifest with very smooth spectra in the estimator, and that fitting them out with polynomials still leaves systematic residuals that are 1-2 orders stronger than the cosmological signal. Besides, the chromatic response of the instrument gives rise to dominant spectral features in the bandpass of the baselines. The short baselines make OWFA a sensitive instrument for rapidly characterising the diffuse foregrounds. In a future paper, we will address further suppression of the foreground residuals.

9 ACKNOWLEDGEMENTS

VRM thanks CTS, IIT Kharagpur, and SC thanks NCRA for hosting them during a part of this work. SC is supported by a University Grants Commission Research Fellowship. The Ooty Radio Telescope is located at Radio Astronomy Centre, Udhagamandalam and operated by the National Centre for Radio Astrophysics, Tata Institute of Fundamental Research.

REFERENCES

- Ali S. S., Bharadwaj S., 2014, *J. Astrophys. Astron.*, **35**, 157
 Ali S. S., Bharadwaj S., Chengalur J. N., 2008, *MNRAS*, **385**, 2166
 Bandura K., et al., 2014, in *Ground-based and Airborne Telescopes V*. p. 914522 ([arXiv:1406.2288](https://arxiv.org/abs/1406.2288)), [doi:10.1117/12.2054950](https://doi.org/10.1117/12.2054950)
 Battye R., et al., 2016, preprint, ([arXiv:1610.06826](https://arxiv.org/abs/1610.06826))
 Begum A., Chengalur J. N., Bharadwaj S., 2006, *MNRAS*, **372**, L33
 Bernardi G., et al., 2009, *A&A*, **500**, 965
 Bernardi G., et al., 2010, *A&A*, **522**, A67
 Bharadwaj S., Ali S. S., 2005, *MNRAS*, **356**, 1519
 Bharadwaj S., Sethi S. K., 2001, *Journal of Astrophysics and Astronomy*, **22**, 293
 Bharadwaj S., Nath B. B., Sethi S. K., 2001, *J. Astrophys. Astron.*, **22**, 21
 Bharadwaj S., Sethi S. K., Saini T. D., 2009, *Phys. Rev. D*, **79**, 083538
 Bharadwaj S., Sarkar A. K., Ali S. S., 2015, *J. Astrophys. Astron.*, **36**, 385
 Bowman J. D., Morales M. F., Hewitt J. N., 2009, *ApJ*, **695**, 183

- Bull P., Ferreira P. G., Patel P., Santos M. G., 2015, *ApJ*, **803**, 21
- Chang T.-C., Pen U.-L., Peterson J. B., McDonald P., 2008, *Physical Review Letters*, **100**, 091303
- Chang T.-C., Pen U.-L., Bandura K., Peterson J. B., 2010, *Nature*, **466**, 463
- Chapman E., et al., 2012, *MNRAS*, **423**, 2518
- Chatterjee S., Bharadwaj S., Marthi V. R., 2017, *Journal of Astrophysics and Astronomy*, **38**, 15
- Chen X., 2011, *Scientia Sinica Physica, Mechanica & Astronomica*, **41**, 1358
- Choudhuri S., Bharadwaj S., Ghosh A., Ali S. S., 2014, *MNRAS*, **445**, 4351
- Choudhuri S., Bharadwaj S., Roy N., Ghosh A., Ali S. S., 2016a, *MNRAS*, **459**, 151
- Choudhuri S., Bharadwaj S., Chatterjee S., Ali S. S., Roy N., Ghosh A., 2016b, *MNRAS*, **463**, 4093
- Condon J. J., 2007, in Afonso J., Ferguson H. C., Mobasher B., Norris R., eds, *Astronomical Society of the Pacific Conference Series Vol. 380, Deepest Astronomical Surveys*. p. 189
- Cress C. M., Helfand D. J., Becker R. H., Gregg M. D., White R. L., 1996, *ApJ*, **473**, 7
- Datta K. K., Choudhury T. R., Bharadwaj S., 2007, *MNRAS*, **378**, 119
- Datta A., Bowman J. D., Carilli C. L., 2010, *ApJ*, **724**, 526
- Di Matteo T., Perna R., Abel T., Rees M. J., 2002, *ApJ*, **564**, 576
- Eisenstein D., 2005, *New Astronomy Reviews*, **49**, 360
- Furlanetto S. R., Oh S. P., Briggs F. H., 2006, *Phys. Rep.*, **433**, 181
- Ghosh A., Bharadwaj S., Ali S. S., Chengalur J. N., 2011a, *MNRAS*, **411**, 2426
- Ghosh A., Bharadwaj S., Ali S. S., Chengalur J. N., 2011b, *MNRAS*, **418**, 2584
- Ghosh A., Prasad J., Bharadwaj S., Ali S. S., Chengalur J. N., 2012, *MNRAS*, **426**, 3295
- Gleser L., Nusser A., Benson A. J., 2008, *MNRAS*, **391**, 383
- González-Nuevo J., Toffolatti L., Argüeso F., 2005, *ApJ*, **621**, 1
- Haslam C. G. T., Klein U., Salter C. J., Stoffel H., Wilson W. E., Cleary M. N., Cooke D. J., Thomasson P., 1981, *A&A*, **100**, 209
- Haslam C. G. T., Salter C. J., Stoffel H., Wilson W. E., 1982, *A&AS*, **47**, 1
- Hinshaw G., et al., 2013, *ApJS*, **208**, 19
- Iacobelli M., et al., 2013, *A&A*, **558**, A72
- Jelić V., et al., 2008, *MNRAS*, **389**, 1319
- Jelić V., et al., 2014, *A&A*, **568**, A101
- La Porta L., Burigana C., Reich P., Reich P., 2008, *A&A*, **479**, 641
- Liu A., Tegmark M., Zaldarriaga M., 2009a, *MNRAS*, **394**, 1575
- Liu A., Tegmark M., Bowman J., Hewitt J., Zaldarriaga M., 2009b, *MNRAS*, **398**, 401
- Liu A., Tegmark M., Morrison S., Lutomirski A., Zaldarriaga M., 2010, *MNRAS*, **408**, 1029
- Liu A., Parsons A. R., Trott C. M., 2014, *Phys. Rev. D*, **90**, 023018
- Loeb A., Wyithe J. S. B., 2008, *Physical Review Letters*, **100**, 161301
- Marthi V. R., 2017, *Journal of Astrophysics and Astronomy*, **38**, 12
- Marthi V. R., Chengalur J., 2014, *MNRAS*, **437**, 524
- McQuinn M., Zahn O., Zaldarriaga M., Hernquist L., Furlanetto S. R., 2006, *ApJ*, **653**, 815
- Morales M. F., Bowman J. D., Hewitt J. N., 2006, *ApJ*, **648**, 767
- Morales M. F., Hazelton B., Sullivan I., Beardsley A., 2012, *ApJ*, **752**, 137
- Owen F. N., Morrison G. E., 2008, *AJ*, **136**, 1889
- Oyama Y., Shimizu A., Kohri K., 2013, *Physics Letters B*, **718**, 1186
- Padmanabhan H., Choudhury T. R., Refregier A., 2015, *MNRAS*, **447**, 3745
- Parsons A. R., Pober J. C., Aguirre J. E., Carilli C. L., Jacobs D. C., Moore D. F., 2012, *ApJ*, **756**, 165
- Patil A. H., et al., 2016, *MNRAS*, **463**, 4317
- Petrovic N., Oh S. P., 2011, *MNRAS*, **413**, 2103
- Pober J. C., et al., 2013a, *AJ*, **145**, 65
- Pober J. C., et al., 2013b, *ApJ*, **768**, L36
- Pober J. C., et al., 2016, *ApJ*, **819**, 8
- Prasad P., Subrahmanya C. R., 2011, *Experimental Astronomy*, **31**, 1
- Pritchard J. R., Loeb A., 2012, *Reports on Progress in Physics*, **75**, 086901
- Pritchard J. R., Pierpaoli E., 2008, *Phys. Rev. D*, **78**, 065009
- Pritchard J. R., Pierpaoli E., 2009, *Nuclear Physics B Proceedings Supplements*, **188**, 31
- Rengelink R. B., Tang Y., de Bruyn A. G., Miley G. K., Bremer M. N., Roettgering H. J. A., Bremer M. A. R., 1997, *A&AS*, **124**
- Rogers A. E. E., Bowman J. D., 2008, *AJ*, **136**, 641
- Santos M. G., Cooray A., Knox L., 2005, *ApJ*, **625**, 575
- Selvanayagam A. J., Praveenkumar A., Nandagopal D., Velusamy T., 1993, *IETE Technical Review*, **10**, 333
- Seo H.-J., Dodelson S., Marriner J., McGinnis D., Stebbins A., Stoughton C., Vallinotto A., 2010, *ApJ*, **721**, 164
- Shaw J. R., Sigurdson K., Pen U.-L., Stebbins A., Sitwell M., 2014, *ApJ*, **781**, 57
- Sirothia S. K., Dennefeld M., Saikia D. J., Dole H., Riquebourg F., Roland J., 2009, *MNRAS*, **395**, 269
- Subrahmanya C. R., Manoharan P. K., Chengalur J. N., 2017, *Journal of Astrophysics and Astronomy*, **38**, 10
- Swarup G., et al., 1971, *Nature Physical Science*, **230**, 185
- Thompson A. R., Moran J. M., Swenson Jr G. W., 2008, *Interferometry and synthesis in radio astronomy*. John Wiley & Sons
- Thyagarajan N., et al., 2013, *ApJ*, **776**, 6
- Thyagarajan N., et al., 2015a, *ApJ*, **804**, 14
- Thyagarajan N., et al., 2015b, *ApJ*, **807**, L28
- Vedantham H., Udaya Shankar N., Subrahmanyan R., 2012, *ApJ*, **745**, 176
- Vernstrom T., 2015, PhD thesis, The University of British Columbia, (2015)
- Villaescusa-Navarro F., Bull P., Viel M., 2015, *ApJ*, **814**, 146
- Visbal E., Loeb A., Wyithe S., 2009, *J. Cosmology Astropart. Phys.*, **10**, 030
- Wang Y., 2006, *The Astrophysical Journal*, **647**, 1
- Wells D. C., Greisen E. W., Harten R. H., 1981, *A&AS*, **44**, 363
- Wieringa M. H., 1991, PhD thesis, Rijksuniversiteit Leiden, (1991)
- Wieringa M. H., 1992, *Experimental Astronomy*, **2**, 203
- Wyithe J. S. B., Loeb A., 2009, *MNRAS*, **397**, 1926
- Wyithe J. S. B., Loeb A., Geil P. M., 2008, *MNRAS*, **383**, 1195

This paper has been typeset from a $\text{\TeX}/\text{\LaTeX}$ file prepared by the author.